

Synergistic Fusion of Aerosol Optical Depth over India from Multi-Sensor Satellite Retrievals with Ground-based Measurements

Shiba Shankar Gouda^{1,2}, Mukunda M. Gogoi¹, S Suresh Babu¹

¹Space Physics Laboratory, Vikram Sarabhai Space Centre, ISRO, Thiruvananthapuram, 695022, India

²Research Centre, Department of Physics, University of Kerala, Thiruvananthapuram, 695034, India

Correspondence: Dr. Mukunda M Gogoi (dr_mukunda@vssc.gov.in)

Abstract

Synergistic fusion of aerosol parameters from multi-sensor measurements is crucial for integrating diverse data sources and generating consistent representations of aerosol distribution for accurate climate impact assessment. In this study, satellite observations from MODIS (Moderate Resolution Imaging Spectroradiometer) and MISR (Multi-angle Imaging SpectroRadiometer) are combined with ground-based measurements from Multi-Wavelength solar Radiometer (MWR) and CIMEL sun-photometers from the ARFINET and AERONET respectively to generate fused Aerosol Optical Depth (AOD) fields over India. The primary focus of this study is to develop a fusion framework over India, involving the evaluation and comparison of two approaches Universal Kriging (UK) and novel hybrid geostatistical-machine learning approach (RK-ML). Both methods share the same geostatistical foundation (variogram-based spatial-modelling) but differ in how the mean structure of AOD is estimated. In UK, satellite-derived AOD serves as deterministic trend for spatial prediction and is effective when ground based observations are well distributed, whereas RK-ML considers SVR-predicted AOD as prior and applies Ordinary Kriging to interpolate residuals from real-time ground observations, maintaining a near-zero residual mean away from observations which reduces distortion under sparse and uneven data conditions. Our results highlight seasonal fused AOD maps (winter, pre-monsoon, and post-monsoon) over India. Leave-One-Out Cross-Validation (LOOCV) is adopted as an evaluation strategy for assessing model performance, showing that the 95% confidence interval ($\pm 2\sigma$) of the fused AOD captures over 80% of ground observations, indicating effectiveness in capturing regional aerosol variability. RK-ML demonstrates more stable spatial patterns and improved LOOCV performance compared to UK, particularly in regions with limited ground-based coverage.

Keywords: Aerosol Optical Depth, Universal Kriging, RK-ML, ARFINET, AERONET, MODIS, MISR

46 **1. Introduction**

47 Atmospheric aerosols play a significant role in introducing uncertainties into climate change
48 projections. Although various factors such as microphysical parameters and chemical
49 composition are important, aerosol optical depth (AOD), quantified by the total amount of
50 columnar aerosol loading in the atmosphere, is the most critical parameter for understanding
51 their climate forcing effects. With advances in technology and retrieval-algorithms, the
52 number of satellites and ground-based observations of AOD is increasing. Although satellites
53 are known to capture spatial heterogeneity of AOD, there could be bias or uncertainty (Huang
54 et al., 2021) compared to ground-based measurements. Even if different satellites observe the
55 same aerosol load over the same region nearly at the same time, the retrieved AOD differs
56 due to the differences in algorithms, calibration, and resolution of the sensors (Kinne, 2009;
57 Schutgens et al., 2020). The geographical complexity also challenges satellites to accurately
58 retrieve AOD over highly heterogeneous land surfaces. On the other hand, data from ground-
59 based sensors, though sparsely distributed, are more reliable than satellite measurements due
60 to improved accuracy of measurement and retrieval procedure (Holben et al., 1998; Moorthy
61 et al., 2007). Thus, the discrepancy between various satellite measurements and between
62 satellite- and ground-based measurements of AOD is a serious concern in accurately
63 characterizing aerosol loading over different parts of the globe (Wong et al., 2013; Sogacheva
64 et al., 2020). In this context, there is a considerable effort in improving aerosol retrieval
65 accuracy using approaches such as synergy processing of sun-photometer and lidar
66 observations (Jin et al., 2025), synergistic retrieval from multi-mission space-borne
67 measurements (Litvinov et al., 2025), gap-filling based on improved tensor-flow-based
68 method (Bai et al., 2024), and the application of physics-informed deep-learning framework
69 to multi-angle polarimetric measurements (Tao et al., 2023). Several studies have reported
70 that if the correlations between the AOD from multiple ground-based and space-based
71 sensors are sufficiently strong (Liu et al., 2004; Jiang et al., 2007; Prasad and Singh, 2007),
72 then these observations can be used together for optimal characterization of aerosol features
73 over a broader region. Thus, there is a growing demand for fused products to address
74 limitations and achieve an optimal outcome, thereby strengthening reliability of aerosol
75 database (Kahn et al., 2023).

76 Several approaches have previously been developed for multi-sensor data fusion involving
77 satellite-to-satellite and satellite-to-ground observations. One notable method is the use of
78 point spread function (PSF) modeling for single scanning footprints (Gupta et al., 2008).
79 While PSF-based techniques are widely applied in image fusion, they face challenges in
80 achieving accurate spatiotemporal collocation across different satellite platforms and don't
81 show applicability regarding ground based AOD fusion rather solely on satellite footprint as a
82 weighting factor for the merging of AOD from different sensors, such as MODIS (Moderate
83 Resolution Imaging Spectroradiometer) and MISR (Multi-angle Imaging SpectroRadiometer)
84 and Clouds and the Earth's Radiant Energy System (CERES). Statistical approaches such as
85 Maximum Likelihood Estimation (Kim et al., 2024; Nirala, 2008) and Bayesian Maximum
86 Entropy (Tang et al., 2016) have been applied to integrate satellite and ground-based
87 observations. These methods explicitly account for uncertainty; but, their practical
88 implementation is often limited by high computational demands, as they require large datasets
89 for effective sampling and detailed pixel-level uncertainty characterization to produce reliable

90 fused products. Similarly, approaches such as the Ensemble Kalman Filter (Li et al., 2020)
91 improve uncertainty quantification and have been applied at the global scale; however, their
92 application is constrained by substantial computational cost and data requirements. These
93 limitations pose challenges for near-real-time applications and for achieving high regional
94 accuracy, particularly in regions with limited ground-based observational support. Simpler
95 least-squares-based approaches, including adaptive weighted estimation (Guo et al., 2013)
96 and semi-empirical optical algorithms (Xu et al., 2012), offer computational efficiency;
97 however, their validation and broader applicability remain uncertain. More recently, machine
98 learning techniques, particularly deep neural networks (DNN) (Kim et al., 2024), have
99 demonstrated comparable performance, but their dependence on large training datasets and
100 challenges in generalization limit their practical deployment.

101 In this study, we have adapted the Kriging technique to produce optimal fused AOD products
102 over India. Among the various data fusion techniques, Kriging has gained significant
103 attention for its applicability under geostatistical framework and has long been recognized as
104 a robust and effective geostatistical technique for spatial estimation (Zimmerman et al., 1999;
105 Shi et al., 2007; Prafull Singh & Verma, 2019; Stein & Corsten, 1991; Zhao et al., 2017).
106 Notably, though geostatistical approaches provide a promising framework for data fusion,
107 they are constrained by high computational demands, particularly when incorporating both
108 spatio-temporal autocorrelation and covariance matrix inversion. Hence, reduced-rank
109 methods such as Spatial statistical data fusion (SSDF) (Puttaswamy et al., 2014; Nguyen et
110 al., 2012) alleviate computational burden but may introduce overfitting due to more number
111 of parameters. Under such a scenario, Universal Kriging (UK) offers more stable AOD
112 estimates near domain boundaries owing to its simpler and more robust formulation
113 (Puttaswamy et al., 2014). Consequently, UK has been widely adopted for multi-sensor
114 fusion integrating satellite and ground-based observations (Chatterjee et al., 2010; Jinnagara
115 Puttaswamy et al., 2014; Lilla and Castrignanò, 2019), although it does not explicitly account
116 for sensor-specific uncertainties. It has been extensively applied and validated across diverse
117 domains within atmospheric research. It has also been utilized for spatial mapping of
118 nutrients over oceans (Zhou et al., 2014) and as well as in mining, hydrology, electro-
119 magnetic field mapping, and remote sensing image processing (Rossi et al., 1994). The
120 Kriging outcomes are also found to be comparable with those from DNN (Chen et al., 2020;
121 Kadow et al., 2020).

122 Previous research over the Indian region has estimated fused AOD from ground and satellite
123 based observations using Cressman method, which employs inverse distance weighting
124 (IDW), a widely used Geostatistical approach (Pathak et al., 2019). In this study, AOD
125 measurements carried out from more than 40 ground-based observatories of the Aerosol
126 Radiative Forcing over India Network (ARFINET; **Fig.-S1a**), which constitutes the national
127 network of aerosol observatories across India and the largest such network in South Asia, are
128 primarily used to integrate with the satellite-based observations from MODIS (Moderate
129 Resolution Imaging Spectrometer) and the MISR (Multi-angle Imaging Spectro-Radiometer)
130 to generate fused AOD using UK framework. Additionally, ground-based AOD data from the
131 AEROSOL ROBOTIC NETWORK (AERONET; **Fig.-S1b**) are utilized to enhance the robustness of
132 the database. While Kriging approaches have been previously applied to generate fused AOD

133 over northern India, the amount of ground data included in their studies was limited (Singh
134 and Venkatachalam, 2014; Singh et al., 2016).

135 While satellite and ground-based AOD measurements generally exhibit a linear correlation,
136 regional and environmental factors introduce biases, noise and nonlinear dependencies
137 between explanatory and response variables. Although nonlinear extensions within the UK
138 framework are possible, they require sophisticated techniques to achieve optimal
139 performance, making the hybrid approach a compelling alternative. While the trend
140 component in UK framework is conventionally modeled using low-order polynomials (e.g.,
141 first or second degree), studies exploring non-linear trend modeling are still relatively rare.
142 For instance, Snepvangers et al. (2003) incorporated a logarithmic trend to improve
143 prediction of soil water content using net precipitation as an auxiliary variable. Freier and
144 Lieres (2015) proposed a Taylor-based linearization technique combined with iterative
145 parameter estimation to capture non-linear trend functions in UK. Freier et al. (2017) further
146 extended this approach to interpolate low-density, irregular biocatalytic data. These
147 techniques are effective when the functional form of the non-linearity is known a priori.
148 However, in most practical scenarios, such explicit formulations are unavailable due to
149 complex, unknown interactions between design factors and responses. In this context,
150 machine learning (ML) models, especially kernel-based methods such as Support Vector
151 Regression (SVR), offer an effective alternative for capturing nonlinear and implicit
152 relationships from data without the need of predefined functional forms. Considering the
153 usefulness of prior spatial information on AOD across the domain, a hybrid Residual Kriging
154 with Machine Learning (RK-ML) framework is adopted in this study, where SVR is used to
155 generate an initial prediction of AOD, which serves as a prior estimate. The preference for
156 SVR over decision-tree-based algorithms arises from its effectiveness for problems involving
157 a small number of features and limited datasets, enabling more reliable fused estimates even
158 when ground-based observations are sparse. While UK involves weighted regression with
159 spatial covariance structures (for spatial predictions), RK-ML employs ML based regression
160 and spatial covariance structure to produce more efficient and stable spatial patterns.

161 In this study, we primarily implement the UK framework over the Indian region to generate
162 monthly fused AOD. Additionally, we evaluate and compare both the geostatistical-machine
163 learning fusion frameworks (UK and RK-ML) while integrating satellite and ground-based
164 AOD observations over India. We further assess the sensitivity of the fusion to the density of
165 ground-based observations, demonstrating how sparse networks can introduce artifacts.

166 **2. Data and Methodology**

167 **2.1 Ground-based AOD**

168 The ground-based AOD is primarily obtained from ARFINET observations, having
169 continuous measurements across the Indian region since 1985 maintained under ISRO-GBP
170 (Gogoi et al., 2009; Babu et al., 2013). The spectral AOD measurements in the ARFINET
171 observatories are carried out using a Multi-Wavelength solar Radiometer (MWR) and the
172 handheld MICROTOPS-II Sun photometer. Both these instruments have been extensively
173 inter-compared, and their consistencies have been established (Kompalli et al., 2010). The
174 MWR is built on the principle of filter wheel radiometry. The measurements of direct solar
175 flux using MWR are made at ten narrow wavelength bands centered at 380, 400, 450, 500,
176 600, 650, 750, 850, 935, and 1025 nm. The AOD is estimated following the Langley

177 Technique (Shaw, 1973; Moorthy et al., 2007; Moorthy et al., 2007) after subtracting the
 178 contribution due to molecular scattering and absorption due to O₃ and water vapour from total
 179 optical depth. For this, the MWR raw data (voltage readings corresponding to the time of
 180 acquisition) for the entire day are split into forenoon and afternoon. If the data span during
 181 each half of the day is more than 3 hours, the Langley plot is made separately for both
 182 forenoon and afternoon following cloud screening criteria. In order to estimate instantaneous
 183 AOD corresponding to each MWR measurement, the time-weighted Langley Intercept (LI)
 184 for the entire day is calculated from the forenoon and afternoon data as

$$185 \quad LI_{\text{daily}} = (LI_{\text{FN}} * T_{\text{FN}} + LI_{\text{AN}} * T_{\text{AN}}) / (T_{\text{FN}} + T_{\text{AN}}) \quad (1)$$

186 Where, T_{FN} and T_{AN} are the durations of MWR measurements in the forenoon and afternoon.
 187 Based on this, the instantaneous AOD (after correcting the contributions due to Rayleigh
 188 scattering, Ozone, and water vapor) is estimated as:

$$189 \quad AOD_{\text{ins}} = \{(LI_{\text{daily}} - \ln V) / m\} - (\tau_{\text{R}} + \tau_{\text{O}_3} + \tau_{\text{WV}}) \quad (2)$$

190 The accuracy of AOD estimates from MWR is based on the accuracy of the estimate of LI.
 191 Since, LI is also a parameter of indirect calibration of the instrument, the temporal variability
 192 of LI is examined to ensure performance of the system and qualify usable data. Typically LI
 193 varies within 5% of the mean and up to 10% in worst cases. Fluctuations are more
 194 pronounced at shorter wavelengths than at longer ones. Owing to these variations, total AOD
 195 uncertainty ranges from 0.02 to 0.03, increasing at shorter wavelengths (<500 nm) and during
 196 high AOD conditions (>0.5), which are mainly limited to the pre-monsoon season.
 197 Importantly, these errors are primarily statistical and uncorrelated across channels, rather than
 198 systematic (e.g., dark current, detector offsets, and molecular scattering/absorption modelling
 199 which are <0.1%). The instrument details, AOD retrieval method, and error budget have been
 200 discussed elsewhere Gogoi et al., 2009; Babu et al., 2013; Kompalli et al., 2010; Moorthy et
 201 al., 2007).

202 Apart from MWR, AOD is obtained from handheld MICROTUPS-II sun-photometer (Solar
 203 Light Company, USA) at five wavelengths (440, 500, 675, 870, and 936 nm). MICROTUPS-
 204 II can achieve AOD estimates with accuracy comparable to CIMEL Sun photometers used in
 205 the AERONET network, with uncertainties ranging from 0.01 to 0.02, as reported by Ichoku
 206 et al. (2002). In addition to ARFINET measurements, simultaneous AOD products (version 3,
 207 level 2.0) available within the study region from AERONET measurements are used. The
 208 CIMEL sun-photometers in AERONET measure AOD at 340, 380, 440, 500, 675, 870, and
 209 1020 nm in a time interval of 5 to 15 min for cloud-free conditions with an uncertainty ~ 0.01
 210 - 0.02 (Eck et al., 1999; Holben et al., 1998; Giles et al., 2019). To use the ARFINET and
 211 AERONET AOD in the fusion experiment, the AOD values are interpolated to 550 nm
 212 (corresponding to MODIS and MISR AOD) using the methodology of Liu et al. (2004):

$$213 \quad \ln \left(\tau_{\lambda_1} / \tau_{\lambda_2} \right) = -\alpha \ln \left(\lambda_1 / \lambda_2 \right) \quad (3)$$

214 Where, τ_{λ_1} and τ_{λ_2} are AODs at wavelengths λ_1 and λ_2 , respectively and α is Angstrom
 215 Exponent. α is determined by applying linear least squares fit to the logarithmic values of
 216 AOD measured at various wavelengths. For this study, values of α were estimated from the

217 wavelength dependent relationship of AOD at 450 and 650 nm for MWR, and 440 and 670
218 nm pair for CIMEL. Using this, AOD at 550 nm was estimated; where the base AOD was
219 taken at 500 nm (in case missing AOD at 500 nm, base AOD at 440 or, 450 nm was
220 considered).

221 **2.2 Satellite retrieved AOD**

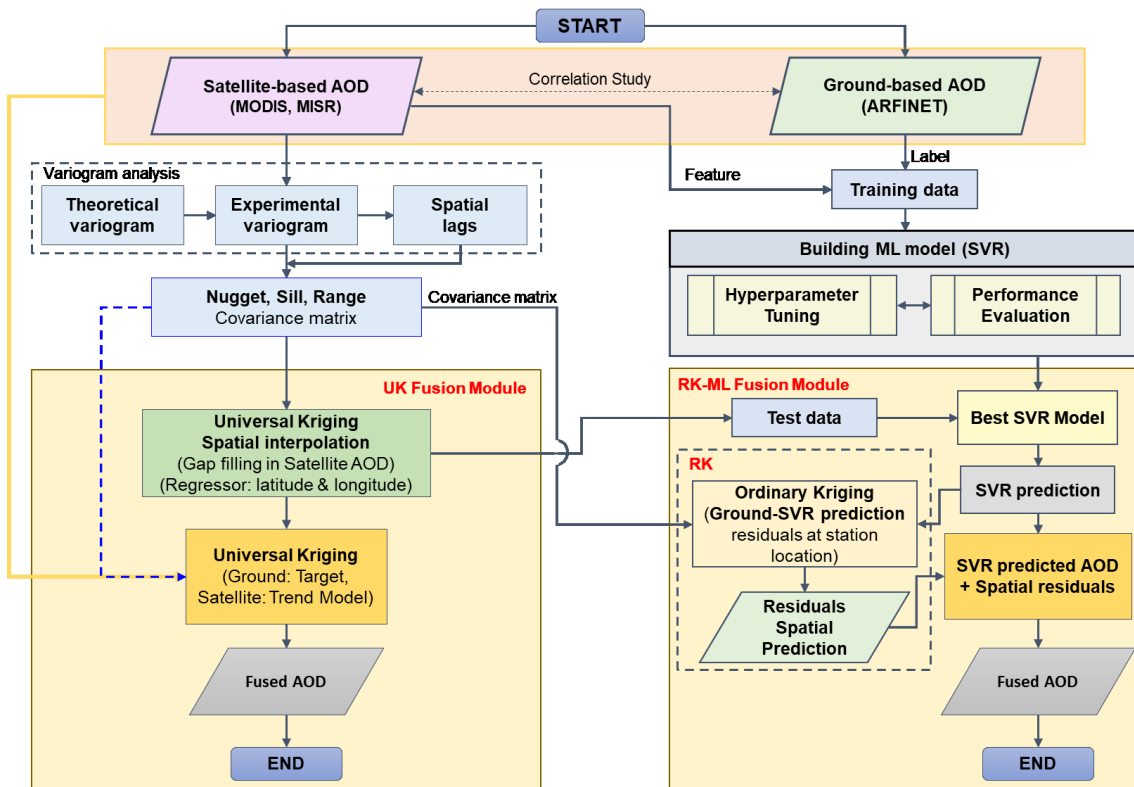
222 The satellite-based AOD for this study is obtained from MODIS and MISR. MODIS data
223 (Collection 6.1 Level-2 AOD at 550 nm; 'AOD_550_Dark_Target_Deep_Blue_Combined';
224 spatial resolution of 10 km; over land) is obtained from NASA's Level-1 and Atmosphere
225 Archive and Distribution System Distributed Active Archive Center (LAADS DAAC). The
226 merged AOD product combines only high-quality Dark Target (DT; QA = 3 over land, QA >
227 0 over ocean) and Deep Blue (DB; QA = 2 and 3) retrievals to provide global 10 km
228 coverage. Over land, selection is based on Normalized Difference Vegetation Index (NDVI),
229 with DB used for bright (arid, semi-arid) surfaces ($NDVI \leq 0.2$), DT for vegetated (darker)
230 regions ($NDVI \geq 0.3$). In transitional zones, the higher-QA retrieval or their average is
231 applied, while over ocean only DT is used. Although this approach improves spatial coverage
232 and usability, uncertainties may arise in averaged regions and due to assumptions about
233 algorithm performance across surface types (Sayer et al., 2014). Sensitivity studies across
234 diverse land surfaces employing various algorithms have validated that integrating the DT
235 and DB methods yields enhanced accuracies, but errors persistently emerge over South Asia
236 (Gao et al., 2021; Tian et al., 2018; Wei et al., 2019). Furthermore, the performance of the
237 product has been evaluated across different seasons (Sharma et al., 2021). Overall, an
238 expected error of $0.05 \pm 0.15 \times AOD$ for DT and $0.05 \pm 0.20 \times AOD$ for DB over the land
239 and $0.03 \pm 0.05 \times AOD$ over the ocean is reported in most studies (Levy et al., 2005; Sayer et
240 al., 2013; Tian et al., 2018; Tian and Gao, 2019; Wei et al., 2019).

241 The MISR AOD (version V23) is obtained from Atmospheric Science Data Centre (ASDC).
242 MISR V23 products provide aerosol information with a spatial resolution of $4.4 \text{ km} \times 4.4 \text{ km}$
243 (Garay et al., 2017; Sayer et al., 2020; Witek et al., 2018, 2021). Theoretical sensitivity
244 studies and performances for MISR (Kahn et al., 2001; Tao et al., 2020) have projected
245 standard deviations of the measurement error associated with optical depth to be $\pm (0.05 +$
246 $20\%AOD_{AERONET})$, showing a consistently narrower range over ocean compared to bright
247 land surfaces.

248 The MODIS and MISR datasets used in this study are both acquired from the Terra satellite
249 platform and therefore have nearly identical overpass times. This temporal consistency
250 ensures improved compatibility in the fusion process and minimizes uncertainties associated
251 with diurnal variability in aerosol loading. In contrast, inclusion of MODIS observations from
252 the Aqua satellite, which has a different overpass time, would introduce additional variability
253 related to diurnal aerosol evolution that requires explicit treatment. Addressing such effects is
254 beyond the scope of the present methodology-focused study and will be considered in future
255 work. In the fusion approach, MODIS AOD represents high-quality retrievals (QA = 2, 3),
256 while MISR exhibits minimal retrieval uncertainties (0.02–0.08) over ground stations.
257 Additional screening or filtering was not applied beyond these criteria, as it may attenuate the
258 inherent systematic bias between ground- and satellite-based observations. Quality-assured
259 and expected-error-based filtering can be considered as part of the future scope of the study to
260 enable more accurate inferences.

261 **2.3 Fusion methodology**

262 The geostatistical data fusion method used in this study combines spatial data from multiple
 263 sources (satellite and ground-based, as detailed in Sections 2.1 and 2.2) with varying
 264 resolutions, accuracies, and types of measurements. The aim is to enhance the overall
 265 understanding and prediction of spatial variables (e.g., AOD) to produce a more accurate and
 266 comprehensive representation of columnar AOD, with an emphasis on reducing inter-sensor
 267 biases through integration with ground-based observations. For this, we have adapted UK
 268 framework, where data interpolation relies on unknown functions (e.g., satellite derived
 269 AOD) represented as trend models with spatial autocorrelation through variogram analysis.
 270 Building on this framework, the fusion methodology is designed to operate under practical
 271 observational constraints, such as differences in sensor characteristics (e.g., spatial coverage,
 272 revisit frequency, and collocation with ground observations), which limit consistent data
 273 availability at daily timescales. Hence, the analysis is conducted at the monthly scale to
 274 improve spatial representativeness, reduce sampling gaps, and enhance statistical robustness.
 275 Notably, the monthly satellite AOD products also retain sensor-specific biases and inter-
 276 product inconsistencies. Thus, the fusion approach presented here is not primarily aimed at
 277 gap-filling, but at generating a more accurate and internally consistent AOD dataset by
 278 integrating complementary information from multiple sensors and ground-based observations.
 279 Thus, even at the monthly scale, the proposed method adds value by reducing retrieval
 280 uncertainties and improving the reliability of aerosol distributions, which is critical for
 281 climate studies and radiative forcing assessments. The overview of the fusion method is
 282 presented in **Fig. 1**, followed by a detailed description of each step in the following sections.



283

284 **Figure 1.** Flowchart of fusion methodology: Universal Kriging (UK) and Residual Kriging
 285 Machine Learning (RK-ML). The machine learning best model is designed based on the long
 286 term MODIS and MISR data which were collocated with ground-based observations.

287 **2.3.1 Correlation analysis**

288 As a first step of the fusion processes, the correlation analysis between the satellite and
289 ground-based AOD was made to understand the association/ biases between the two data sets
290 at different spatiotemporal scales. This is useful to understand the requirement of multi-sensor
291 data fusion. For this, a statistical spatio-temporal matching approach similar to those reported
292 elsewhere by Basart et al., (2009); Chu et al., (2002); Filonchyk et al., (2019); Ichoku et al.,
293 (2002) was applied, in which satellite observations were spatially averaged at 0.5° spatial
294 resolution and compared with ground-based AOD averaged within a 30 minute time window
295 around the overpass time of the TERRA satellite which accommodated 14 to 15
296 measurements from MWR (data frequency 2 min) and 1 to 2 measurements from CIMEL
297 (data frequency 15 min) observations. Although satellite products such as MODIS (~ 10 km)
298 and MISR (~ 4.4 km) provide higher spatial resolution potentially capturing finer regional
299 variability in aerosol distributions, yet their direct comparison with ground-based point
300 measurements introduces representativeness errors due to scale mismatch. Aggregating the
301 data to a coarser grid (0.5°) reduces this mismatch by ensuring that both satellite and ground
302 observations represent comparable spatial scales, thereby improving the robustness of
303 validation and fusion. Thus, the choice of 0.5° represents an optimal choice, yielding higher
304 correlation and lower root mean square error (RMSE) (**Figs. S2a, b**), in addition to retaining
305 regional variability and ensuring sufficient data density within each grid cell for stable
306 statistical estimation and fusion. The consideration of 0.5° resolution is in line with approach
307 adopted by Tandule et al. (2026) for retrieving AOD from satellite observations, ensuring
308 improved representativeness and temporal consistency in comparisons between satellite-
309 derived and ground-based AOD. In addition, generating AOD at this resolution provides a
310 valuable reference dataset for comparison and validation against reanalysis products and
311 model outputs of AOD, where satellite observations are commonly assimilated as primary
312 inputs. Further, AOD observations in this study were aggregated to a monthly scale to ensure
313 more consistent spatial coverage and improve the reliability of multi-sensor fusion analysis.
314 Due to the differences in spatial coverage and revisit characteristics of MODIS and MISR as
315 well as temporal gaps in data availability from ground-based instruments (**Figs. S3a, 3b, 3c**),
316 daily datasets often contained substantial spatial gaps over the study domain.

317 **2.3.2 Variogram Analysis**

318 Variogram analysis is used to quantify and model the spatial autocorrelation (i.e., spatial
319 dependence) of a dataset. It evaluates how the spatial variability between data points changes
320 as a function of lag distance, the distance separating two sample points in space. To capture
321 the spatial dependency of the data, geographical parameters such as latitude, longitude, and
322 elevation are often incorporated as covariates in the trend function, thereby incorporating the
323 spatial context of the sampling locations. This approach has been widely applied in studies
324 involving meteorological parameters (Chua and Bras, 1982; Holdaway, 1996; Nalder and
325 Wein, 1998). In the present context, spatial representation of AOD is fairly represented as a
326 trend function comprising of latitude, longitude, and elevation, which serve as proxies for
327 underlying spatial variations of geographical and atmospheric influences that significantly
328 affect aerosol distribution. However, it is important to note that most geostatistical methods,
329 such as Kriging, assume the underlying field to follow second order or, intrinsic stationarity
330 (mean is constant, and the covariance or, variance of increments depends only on spatial lag).

331 However, real-world environmental and geophysical data often exhibit large-scale spatial
 332 trends driven by physical and geographical factors, such as latitude, longitude, and elevation.
 333 In the case of AOD, these variables act as key spatial predictors that capture dominant
 334 regional gradients and can be used to model and remove the large-scale spatial trend. In the
 335 presence of strong spatial trends, variogram may become unbounded or exhibit unrealistically
 336 large ranges. These spatial trends violate the stationarity assumption which can lead to
 337 unbounded variogram. To address this spatial detrending of the data is performed, which
 338 isolates the local fluctuations or residuals from the spatial data set. This serves as an essential
 339 step in geostatistical analysis to ensure a well-defined and bounded variogram, enabling
 340 reliable estimation of sill, nugget, and range parameters for spatial covariance modeling. To
 341 validate this assumption, we obtained the frequency distribution of satellite AOD and their
 342 residuals (**Fig. S4**) after detrending. A nearly symmetric histogram of detrended residuals
 343 indicates that the trend component has been effectively removed, which is a prerequisite for
 344 second-order stationarity (Tang et al., 2016). Since the detrending in our study is purely a
 345 spatial operation, the temporal dimension is not explicitly considered and is effectively
 346 treated as constant during the detrending process. Consequently, the approach does not
 347 involve long-term datasets or explicitly account for seasonal variability (e.g., all four
 348 seasons).

349 The semivariance, which measures the degree of spatial variability between pairs of sample
 350 points as a function of their separation distance, known as the lag-distance (h), is calculated
 351 as:

$$352 \quad \gamma(h_x) = 1/2n(h) (\sum [z(x_i) - z(x_i + h)]^2) \quad (4)$$

353 Where $z(x_i)$ and $z(x_i+h)$ are the values of the variables of interest at locations x_i and $x_i + h$ (= x_j), respectively; $n(h)$ is the number of pairs of points separated by the lag-distance h , which
 355 is given as:

$$356 \quad h_x = r \cos^{-1}(\sin \varphi_i \sin \varphi_j - \cos \varphi_i \cos \varphi_j \cos(\theta_i - \theta_j)) \quad (5)$$

357 Where $\varphi_{i,j}$ represent longitudes of locations x_i and x_j , and $\theta_{i,j}$ represent latitudes of locations
 358 x_i and x_j ; r is the mean radius of the earth. Following this, the empirical variogram is
 359 calculated from the actual observational data, showing the relationship between semivariance
 360 and lag distance for each set of observations. The experimental variogram is obtained after
 361 binning semivariance at certain lags of the empirical variogram. The experimental variogram
 362 is then fitted with a theoretical model to describe the spatial continuity of the variable. The
 363 theoretical models considered in the present study include Exponential, Spherical, and
 364 Matheron models; the mathematical expressions are given as:

$$365 \quad \gamma_{theo}(h_x) = \begin{cases} 0 & h_x = 0 ; \\ \sigma_n^2 + \sigma_b^2 (1 - \exp(-h_x/l)) & h_x > 0 \end{cases} \quad \text{(Exponential)} \quad (6)$$

$$366 \quad \gamma_{theo}(h_x) = \begin{cases} 0 & h_x = 0 ; \\ \sigma_n^2 + \sigma_b^2 \left(3h_x/2l - 1h_x^3/2l^3 \right) & 0 < h_x \leq l ; \\ \sigma_n^2 + \sigma_b^2 & h_x > l \end{cases} \quad \text{(Spherical)} \quad (7)$$

$$367 \quad \gamma_{theo}(h_x) = \begin{cases} 0 & h_x = 0; \\ \sigma_n^2 + \sigma_b^2 \left(1 - \exp\left(-h_x^2/l^2\right) \right) & h_x > 0; \end{cases} \quad \text{(Matheron)} \quad (8)$$

368 In the above equations, $\sigma^2 = \sigma_n^2 + \sigma_b^2$, represents the total variance observed in AOD data at
369 larger lag distances (spatially uncorrelated AOD data). σ_n^2 is nugget (y-intercept of the
370 variogram), which represents the semivariance at a very small lag distance, approaching zero.
371 Nugget (spatial variation at distances smaller than the smallest sampling interval) is indicative
372 of the presence of measurement error or noise in the data. A large nugget relative to the sill
373 (i.e., the semivariance value where the variogram levels off, representing maximum
374 variability or correlation between data points at a given spatial distance) suggests significant
375 measurement error or unresolved variability. This can indicate potential issues with data
376 quality. On the other hand, a small nugget implies that the data is relatively free of noise and
377 that most of the spatial variability is due to the structured spatial process. σ_b^2 is variance in
378 spatially correlated data, and this parameter gradually increases with increasing lag distances
379 until it reaches sill. l is the range parameter, the distance at which the semivariance reaches
380 the sill; up to this distance, data are spatially correlated with each other. The higher the range,
381 the more similar the values are at greater distances from each other. The spatial covariance
382 function can be derived from the variogram model as:

$$383 \quad C_{ij} = \sigma^2 - \gamma_{theo} \quad (9)$$

384 2.3.3 Universal Kriging

385 Universal Kriging (UK) also referred to as Kriging with a trend model, extends Ordinary
386 Kriging by incorporating a deterministic trend component alongside the stochastic spatial
387 component. This approach is useful when there is an underlying trend in the data that varies
388 across the study area. The UK method uses both the spatial autocorrelation structure and the
389 deterministic trend to make predictions. The UK model can be expressed as:

$$390 \quad Z = M_z\beta + \epsilon \quad \text{Or, } \epsilon = Z - M_z\beta \quad (10)$$

391 Where, $Z = [Z(x_1), Z(x_2), \dots, \dots, Z(x_n)]^T$ represent the values of the variables of interest at
392 locations x_1, x_2, \dots, x_n , respectively. M_z is the deterministic trend component of the model
393 ($n \times p$) where p is representing the number of regressors; and β is the unknown drift
394 coefficient ($p \times 1$) to be estimated; ϵ is the stochastic component or stochastic residuals
395 ($n \times 1$), i.e., mean zero random fields.

396 In the present study, the trend component M_z for fusion is defined as

$$397 \quad M_z = \begin{pmatrix} 1 & MODIS_{AOD_1} & MISR_{AOD_1} \\ 1 & MODIS_{AOD_2} & MISR_{AOD_2} \\ \vdots & \vdots & \vdots \\ 1 & MODIS_{AOD_n} & MISR_{AOD_n} \end{pmatrix} \quad (11)$$

398 This is similar to a multiple regression model, which is described through a combination of a
399 constant term and two sensor measurements that act as regressors to predict AOD at
400 estimation locations. The first component of this trend model represents the overall offset
401 (i.e., the mean of the portion of the AOD distribution that is not captured by MISR and

402 MODIS). This constant term thereby represents any systematic offset between the combined
 403 (MISR and MODIS) satellite-retrieved AOD and the ground-measured AOD.

404 Following equation (10), the expected value at prediction locations (x_s) can be expressed as
 405 the best linear unbiased prediction (BLUP):

$$406 \hat{Z}(x_s) = m_s^T \hat{\beta} + C_{zs}^T C_{zz}^{-1} (Z - M_z \hat{\beta}) \quad (12)$$

407 Here, $C_{zs}(n \times s)$ is the spatial covariance matrix of the residuals between the sample location
 408 (i.e., measurement locations) and prediction locations (i.e., estimation locations) and $C_{zz}(n \times$
 409 $n)$ is the spatial covariance matrix of the residuals between the sample locations (i.e.,
 410 measurement locations) as obtained from equation (9). The unknown coefficient $\hat{\beta}$ can be
 411 expressed as the generalized least squares (GLS) estimator from the covariance matrix,

$$412 \hat{\beta} = (M_z^T C_{zz}^{-1} M_z)^{-1} M_z^T C_{zz}^{-1} Z \quad (13)$$

413 Alternatively, minimizing the mean square error (MSE) of all predictions among the
 414 predictors of the form $\lambda^T Z$ subjected to unbiasedness constraint, i.e., $E(\lambda^T Z) = E(Z(x_s))$ for
 415 all β , which is identical to $\lambda^T M_z \hat{\beta} = m_s^T \hat{\beta}$ and under conditions for minimizing variance
 416 ($\lambda^T Z - Z$), Lagrange multipliers ($\mu(p \times s)$) are used to solve the linear constraint equations
 417 as given below,

$$418 \begin{bmatrix} C_{zz} & M_z \\ M_z^T & 0 \end{bmatrix} \begin{bmatrix} \lambda \\ \mu \end{bmatrix} = \begin{bmatrix} C_{zs} \\ m_s \end{bmatrix} \quad (14)$$

419 Here, $M_z(n \times p)$ and $M_z^T(p \times n)$ are trend models of AOD given by equation (11); m_s
 420 ($p \times s$) is trend model at s estimation locations; $\lambda(n \times s)$ are the Kriging weights, μ is the
 421 Lagrange multiplier.

422 The system of equations is solved for Lagrange multiplier μ and weights λ to estimate AOD
 423 at estimation locations. This can be expressed as:

$$424 \begin{bmatrix} \lambda \\ \mu \end{bmatrix} = \begin{bmatrix} C_{zz} & M_z \\ M_z^T & 0 \end{bmatrix}^{-1} \begin{bmatrix} C_{zs} \\ m_s \end{bmatrix} \quad (15)$$

$$425 \lambda = \{C_{zz}^{-1} - C_{zz}^{-1} M_z (M_z^T C_{zz}^{-1} M_z)^{-1} M_z^T C_{zz}^{-1}\} C_{zs} + C_{zz}^{-1} M_z (M_z^T C_{zz}^{-1} M_z)^{-1} m_s \quad (16)$$

$$426 \lambda^T Z = C_{zs}^T C_{zz}^{-1} (Z - M_z \beta) + m_s^T \beta \quad (17)$$

427 The prediction variance associated with predicted values can be represented as

$$428 \text{Var}(Z(x_s) - \hat{Z}(x_s)) = \sigma_{Z(x_s)}^2 - C_{zs}^T C_{zz}^{-1} C_{zs} + (m_s^T - (M_z^T C_{zz}^{-1} C_{zs})^T)^T (M_z^T C_{zz}^{-1} M_z)^{-1} (m_s^T - (M_z^T C_{zz}^{-1} C_{zs})^T) \quad (18)$$

429 The above weighting approach determines the values at prediction locations. Our foremost
 430 approach involved creating a trend model for fusion. For this purpose, we generated a
 431 complete satellite-based map of AOD from MODIS and MISR separately over the study
 432 region using the UK method. In this framework, geographical parameters such as latitude,
 433 longitude and elevation are treated as regressors (trend model), whereas observed satellite
 434 data serve as response variables to fill the gaps in individual satellite datasets. Subsequently,
 435 in the final spatial fused predictions, the ground-based AODs were treated as the response
 436 variables, where the satellite data, along with the elevation model (used as additional
 437 information), were used as regressors.

438

439 2.3.4 Residual Kriging Machine Learning (RK-ML)

440 The RK-ML approach is implemented in this study through a hybrid approach to generate
 441 reliable estimates of fused AOD, with improved predictive accuracy using a limited of
 442 ground-based observations. Although UK and the proposed RK-ML approach appear
 443 methodologically different, they share a common conceptual foundation. From a generalized
 444 regression perspective, both methods rely on a covariance structure to characterize spatial
 445 dependence among grid points. However, when the number of observations is limited, the
 446 statistical parameters in UK can adversely affect predictions at estimation locations. To
 447 overcome the limitations associated with limited observations, SVR is employed due to
 448 robustness of its regularized formulation in both regression and classification tasks (Sifaou et
 449 al., 2021), where predictions are learned from datasets within a historical training window.
 450 These predictions provide prior information on ground-based AOD that is independent of the
 451 spatial configuration of the current ground based-observations.

452 The best-performing SVR model is first identified based on a time window of five years of
 453 data (simultaneous MODIS, MISR and ground measurements) for a specific month (season)
 454 targeting consistent aerosol conditions. Subsequently, this model leverages spatially
 455 interpolated features from MODIS and MISR data (gap filled AOD by UK) to generate SVR-
 456 predicted maps to obtain a full generalized AOD map for that month. The discrepancies
 457 between SVR-predicted values and observed ground measurements are treated as residuals,
 458 which are then spatially modeled using Ordinary Kriging. The resulting residual predictions
 459 are combined with SVR outputs to produce RK-ML-based fused products. This approach
 460 provides a robust alternative to traditional UK-based data fusion techniques by capturing
 461 complex relationships between predictors and target variables. The detailed RK-ML
 462 methodology is given below.

463 SVR transforms features into a higher-dimensional space, making them linearly separable and
 464 helps improving the prediction of target variables like ground based AOD. The use of SVR in
 465 Kriging has been reported in previous studies to improve model predictions (Wang et al.,
 466 2008; Baisad et al., 2023). The SVR model is represented by:

$$467 Z_{svr} = w^T \varphi + b \quad (19)$$

468 where φ is the kernel transformed input features, w is the nonzero vector normal to
 469 hyperplane (the plane or decision boundary that best fits the n dimension input vectors while
 470 maintaining a margin of tolerance (ε -insensitive zone) around it) and $b \in \mathbb{R}$. This expression
 471 assumes that Z_{svr} exist when it approximates all $w^T \varphi$ with ε precision for linearly separable
 472 data. Along with it, the concept of soft margin loss function is considered which introduces
 473 slack variable ξ (+ve) and ξ^* (-ve) to allow some points lying inside the hyperplane.

474 Hence the optimization problem is subject to minimization of

$$475 \frac{1}{2} \|w\|^2 + C \sum_{i=1}^l (\xi + \xi^*) \quad \text{Such that} \begin{cases} Z - w^T \varphi - b \leq \varepsilon + \xi \\ w^T \varphi + b - Z \geq \varepsilon + \xi^* \\ \xi_i \xi_i^* \geq 0 \end{cases} \quad (20)$$

476 The regularization constant C trades off between the model complexity and empirical error up
 477 to which deviations larger than ε can be tolerated. ξ , ξ^* are regression errors. The detailed
 478 explanation of SVR model is available in the literature (Smola & Schölkopf, 2004; Brereton

479 & Lloyd, 2010). In the present study, best model of SVR is decided from the minimum
 480 RMSE between predicted AOD and real AOD after tuning its hyperparameters.

481 The residuals, which are the difference between collocated AOD of SVR predictions from
 482 ground based AOD, are estimated from the difference between $\hat{Z}_{svr}(x_s)$ and Z , *i.e.*,
 483 $\hat{Z}_{svr}(x_s) - Z$. These residuals under ordinary Kriging are modeled as $\delta(s) = \mu +$
 484 $\varepsilon(s)$ where μ refers to the mean values of residuals over study domain, which resembles
 485 similar mathematics of universal Kriging, except M_z & $m_s = 1$ (eq. (10) to eq. (17)).
 486 Following this, the estimated residuals at unknown locations are determined as

$$487 \quad \delta(x_s) = \lambda^T \delta(x_z)$$

488 The weighting parameter λ is obtained from the covariance matrices as follows

$$489 \quad \begin{bmatrix} \lambda \\ \mu \end{bmatrix} = \begin{bmatrix} C_{zz} & 1 \\ 1 & 0 \end{bmatrix}^{-1} \begin{bmatrix} C_{zs} \\ 1 \end{bmatrix} \quad (21)$$

490 The ordinary Kriging estimation contains the spatial relation while the SVR prediction
 491 contains the optimal estimations from features (Satellite) and labels (Ground AOD). The final
 492 fused map can then be estimated as

$$493 \quad Z = \delta(x_s) + Z_{svr}(x_s) \quad (22)$$

494 The hyperparameters of the SVR model were optimized using a grid-search strategy as part of
 495 the training process. In this approach, predefined values for key hyperparameters - such as the
 496 regularization parameter (C), kernel type, gamma (Y) and epsilon (ε) - were combined to
 497 form all possible parameter configurations, and each configuration was evaluated. For every
 498 hyperparameter combination, model performance was assessed using the negative mean
 499 squared error (neg-MSE) as the evaluation metric. This metric quantifies prediction error, and
 500 allows selection of the best model by maximizing the score. Due to the limited size of the
 501 dataset, leave-one-out cross-validation (LOOCV) was used during training instead of k-fold
 502 cross-validation. Even though other cross-validation approaches, such as site-based, temporal,
 503 or sample-based validation, can also be used to assess model robustness, the LOOCV was
 504 considered the most suitable approach in this study considering the limited number of
 505 samples and the uneven spatial distribution of ground observations. In LOOCV, the model is
 506 trained repeatedly on all samples except one, which is used for validation. This procedure is
 507 repeated so that each data point serves once as the validation sample. This approach
 508 maximized the use of available data while providing an unbiased estimate of model
 509 performance. Based on this procedure, a linear kernel was identified as the optimal choice for
 510 the RK-ML models, which were subsequently evaluated on independent test sets (20% for
 511 MODIS, N=318; 10% for MISR, N=71). For MODIS AOD features, the best model
 512 configuration was C = 1, gamma = 'scale', kernel = 'linear'; for MISR AOD features, the
 513 optimal configuration was C = 100, gamma = 'scale', kernel = 'linear'. The use of a linear
 514 kernel suggests a predominantly linear relationship between satellite observations and
 515 ground-based AOD. Inclusion of the regularization parameters C and gamma controls
 516 overfitting and penalizes noisy inputs, enabling the ML framework to generate more reliable
 517 estimates. These estimates were further corrected using spatial residuals from RK, allowing
 518 RK-ML to outperform UK under conditions of limited or biased AOD observations. The final
 519 models were evaluated using correlation coefficient (R), R², mean absolute error (MAE), and

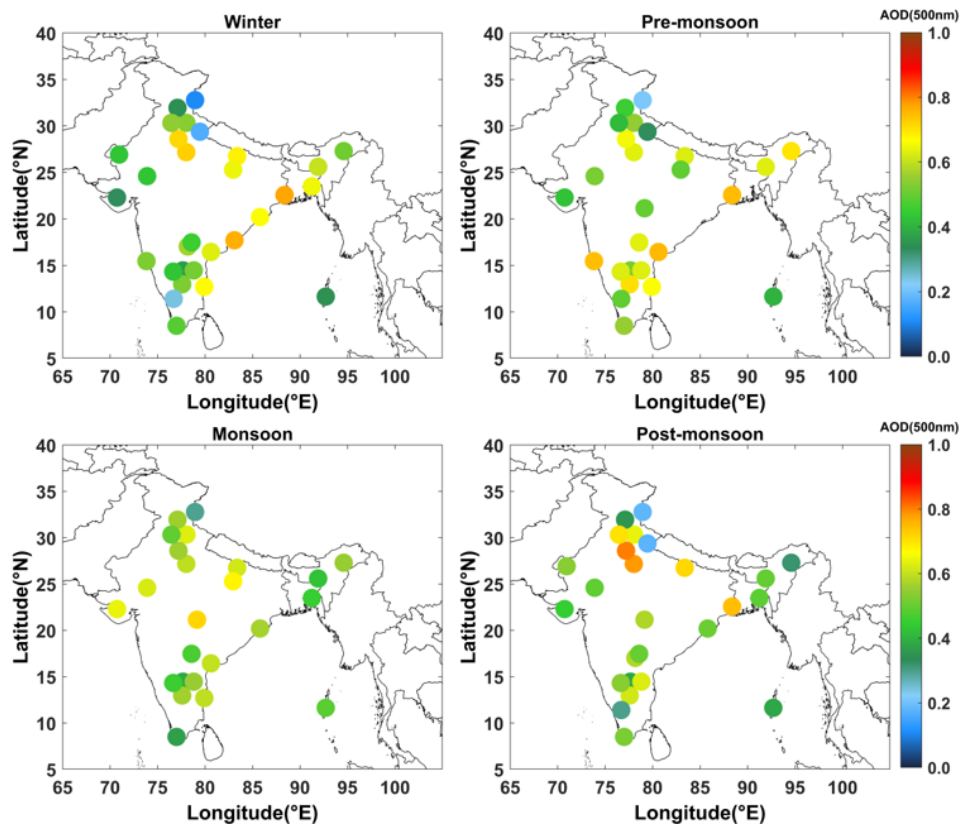
520 RMSE on both training and test sets (**Table ST1**). Results indicate that training and test
521 performances were comparable (with training R^2 values either lower or close to test R^2),
522 correlation coefficients were consistently high, and errors (RMSE, MAE) were low. These
523 outcomes confirm that the SVR models did not suffer from overfitting and generalized well to
524 unseen data, despite the limited sample size.

525 Although other machine learning algorithms, such as Random Forest (RF) and XGBoost, can
526 also be integrated within the RK-ML framework, a sensitivity analysis conducted on MODIS
527 test dataset indicated that SVR achieved comparable or better performance metrics (R ,
528 RMSE; Supplementary Fig. S5).

529 3. Results and discussions

530 3.1 Regional distribution of AOD from ground-based and satellite observations

531 The analysis of spatial distribution of AOD is crucial for understanding the consistency of
532 measurements across different sensors. The large-scale spatial variations in the data help
533 identify overall spatial trends over latitude-longitude and geographic elevation. Emphasizing
534 spatial trends is also critical for assessing the mathematical assumptions underlying Kriging
535 and variogram analysis, which rely on the condition of second-order stationarity within the
536 sampled data. In view of this, ground-based AOD at 500 nm was considered for long-term
537 comparison of MODIS and MISR AOD at 550 nm as the closest approximation. The typical
538 AOD patterns over different regions over India from ground-based measurements, derived
539 from 10 years of measurements from the ARFINET database using MWR and Microtops
540 instruments, is illustrated in **Fig. 2**.



541

542 **Figure 2.** Long-term (2011-2020) ground-based AOD at 500 nm from MWR and
543 MICROTOPS-II measurements in the ARFINET over the Indian region. The seasons are

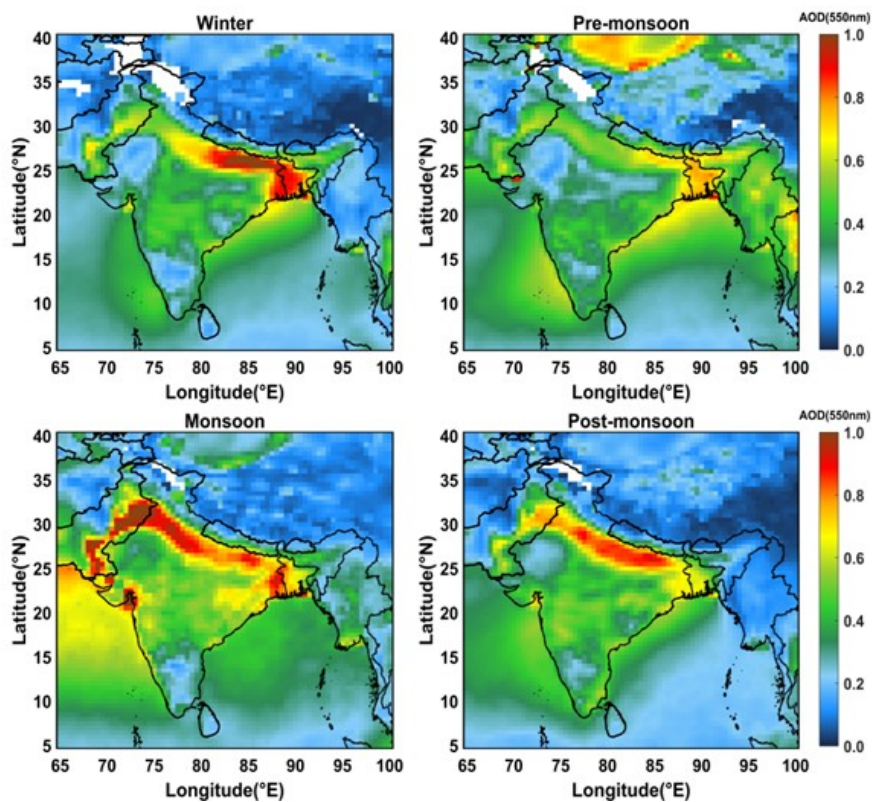
544 winter: December, January, February (DJF); Pre-monsoon: March, April, May (MAM);
545 Monsoon: June, July, August, September (JJAS); Post-monsoon: October, November (ON).
546 The different regions considered for representing Indo-Gangetic plane (IGP), North-west
547 (NW), North-east (NE), Peninsular India (PI), and Central India (CI) is provided (**Fig. S6**).

548 Various factors such as the dominance of natural and anthropogenic sources, local and
549 synoptic meteorology cause observed spatio-temporal variations in AOD at a particular
550 location. Over most of the locations in the Indo-Gangetic Plains (IGP), AOD shows
551 consistent high values (> 0.6) throughout different seasons. This is similar to the observations
552 reported by Lodhi et al., (2013); Singh et al., (2020); Tiwari et al., (2018). Next to the IGP,
553 the north-eastern (NE) India experiences higher AOD with peak during the pre-monsoon
554 season. Similar pattern is reported elsewhere (Gogoi et al., 2009). In Peninsular India (PI),
555 AOD is highest during the pre-monsoon period, followed by a significant reduction during
556 the summer monsoon. This is similar to the earlier studies by Kalluri et al., (2016); Kumar et
557 al., (2009); Sinha et al., (2013); Vachaspati et al., (2018).

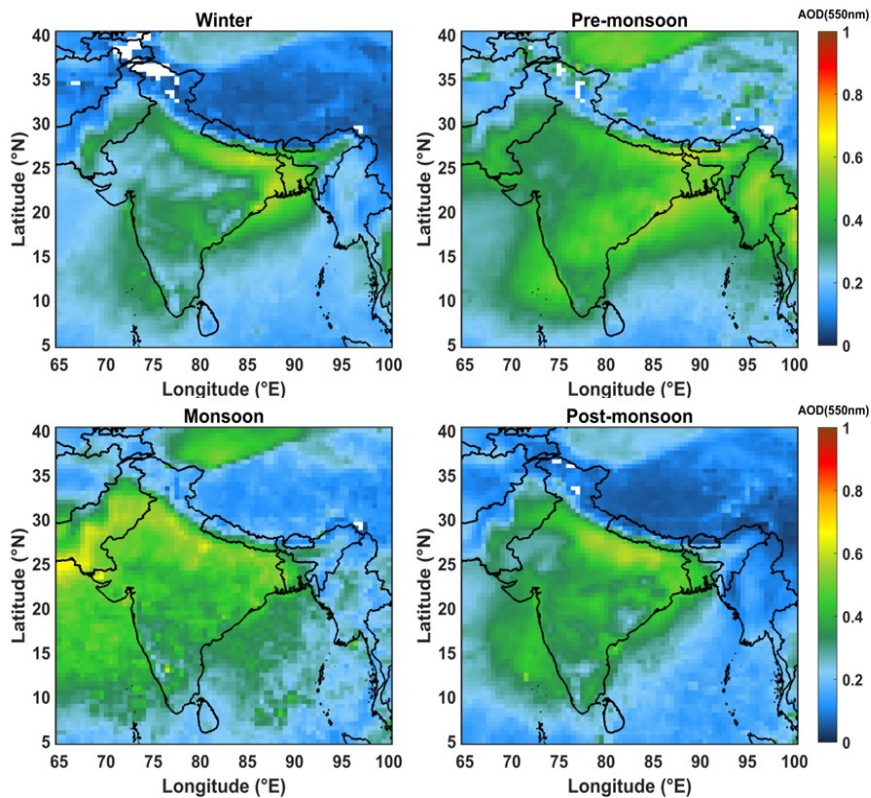
558 The spatial patterns of a decadal average satellite-based MODIS and MISR AOD (2011–
559 2020; **Fig. 3a, 3b**) also shows persistent high AOD values in the IGP and its outflow regions
560 across all seasons. In PI, the presence of elevated mountain ranges such as the Western and
561 Eastern Ghats, coupled with its proximity to the Indian Ocean, results in regional-scale AOD
562 variability. During the pre-monsoon and monsoon periods, oceanic and coastal regions
563 exhibit higher AOD levels compared to the winter and post-monsoon periods. Though
564 dominant spatial patterns are same in long term AOD from spaceborne sensors and their
565 differences with ground-based AOD over same spatial grids are minimal (**Figs. S7a, b**), the
566 discrepancy persists, especially over northern India and during monsoon period. As cloud-
567 haze misclassifications may act as one of the factors from the observed differences between
568 satellite and ground AOD in the monsoon periods, haze-removal criteria (following Jiao et
569 al., 2023) to MODIS AOD was applied. A significant impact of haze over the peninsular
570 region is seen during monsoon (Supplementary **Figs. S7c, d**), however, it shows negligible
571 influence during the other seasons. This is clearly seen from the difference maps between the
572 MODIS and ground-AOD over different ground locations, showing minimal changes before
573 and after the haze removal. This exercise suggests that cloud-haze misclassification is not the
574 primary factor driving the observed differences, except under monsoon conditions. Under
575 such a scenario, localized discrepancies may arise due to spatial sampling limitations of the
576 ground- based observations. As the ARFINET stations are sparsely and unevenly distributed,
577 particularly across regions of high aerosol loading in northern India, this may result in the
578 apparent lack of complete regional representation of ground observations. Additionally,
579 discrepancies between MODIS and MISR AOD are also seen owing to fixed and multi angle
580 retrievals especially in Pre-monsoon period over the NW region, where MISR AOD is
581 significantly different from MODIS. There are also some pockets where low AOD region
582 observed by MODIS is alternatively represented as a region of higher AOD in MISR
583 observations, particularly in proximity to the IGP outflow. Previous studies over similar
584 geographic regions have indicated that the frequency of observations, cloud masking, and
585 geographical factors impact both MODIS and MISR observations, stemming from algorithm
586 assumptions related to cloud masking and SSA. Overall, the spatial patterns of AOD from
587 ground and satellite observations reveal the following:

- 588 • During the pre-monsoon period, northern India experiences increased AOD.
- 589 • During the winter season, cold temperatures, a low boundary layer height, and humid
590 air create hazy conditions with high AOD (Nair et al., 2020). Along with it, winds
591 over the IGP are mostly north-westerly, with an anti-cyclonic pattern over central
592 India, driving aerosols to peninsular region.
- 593 • The post-monsoon AOD also remains high, similar to winter levels, particularly in the
594 IGP due to biomass burning (Kumar et al., 2012; Lodhi et al., 2013; Subba et al.,
595 2021).
- 596 • The spatial patterns of AOD across different seasons are well captured by both
597 satellite and ground-based observations. However, notable differences exist between
598 ground-based and MODIS and MISR AOD. While MODIS tends to overestimate
599 AOD over the IGP, it generally underestimates AOD over the PI, NE, and NW
600 regions. MISR significantly underestimates higher AOD regions.

601 Despite the above constraints, the general agreement in magnitude and temporal variability
602 supports the reliability of both datasets for the fusion framework. Thus, our approach
603 explicitly accounts for such discrepancies by integrating the broad spatial coverage of satellite
604 observations with the higher accuracy of ground-based measurements. In this context, ground
605 observations are treated as local constraints rather than complete spatial representations,
606 thereby minimizing the influence of regional sampling gaps in the ground network.
607 Consequently, the final fused AOD represents a bias-corrected satellite-derived field
608 constrained by ground observations.



609 **Figure 3a.** Long-term (2011-2020) satellite based AOD (at 550 nm) from MODIS over
610 south-Asian region.
611



612
 613 **Figure 3b.** Long-term (2011-2020) satellite based AOD (at 550 nm) from MISR over south-
 614 Asian region.

615 **3.2 Inter-comparison of satellite- and ground-based AOD**

616 Having examined the spatial distribution, a quantitative evaluation of the associations or
 617 biases between satellite and ground-based AOD at different periods is examined for the years
 618 2012, 2016, and 2021. The three different years were selected such that way that the AOD for
 619 2012 and 2021 provides the decadal variability, while 2016 represents an intermediate period
 620 between these two years, enabling us to better assess the progression and variability of AOD
 621 over a long period. The scatter plots (Supplementary **Figs. S8-S10**; the number of ground
 622 stations included in the correlation studies is given in **Table 1**) between MODIS/ MISR and
 623 ground-based AOD highlight moderate to strong correlations ($\sim 0.8-0.9$) in winter (January)
 624 and post-monsoon (November), while moderate correlations ($\sim 0.54-0.77$) between the two
 625 are observed in pre-monsoon (May). The RMSE between MISR and ground-based AOD is
 626 higher (≥ 0.2) during winter and post-monsoon, whereas higher RMSE values between
 627 MODIS and ground-based AOD are observed during the pre-monsoon period. The prominent
 628 locations contributing to mean errors and weak correlations with ground observations are
 629 situated in the NW and IGP regions.

630 The quartile-plots (**Figs. S11-S13**) highlight significant spatio-temporal variability in AOD,
 631 with both sensors displaying higher AOD over terrestrial regions, particularly in the IGP, its
 632 outflows, and South (Peninsular) and Central India. The third and fourth quartiles are more
 633 representative for AOD over land regions than in surrounding areas like oceans and elevated
 634 terrain. Data with respect to longitude and latitude show that higher AOD values are mostly
 635 confined to $20^{\circ}-30^{\circ}\text{N}$ latitude and $80^{\circ}-95^{\circ}\text{E}$ longitude. However, MODIS consistently
 636 recorded significantly higher AOD values than MISR, with notable dissimilarities in quartile
 637 patterns over northern India during May.

638 Both the correlation and quartile analyses highlight the advantages and limitations of MODIS
639 and MISR observations. For example, MISR tends to underestimate high AOD conditions in
640 urban regions compared to MODIS, even though it can effectively separate surface
641 contributions under low aerosol loading, as also reported by Tao et al. (2020). Under high
642 AOD conditions, the benefit of multi-angle measurements becomes limited, as thick aerosol
643 layers smooth out surface reflectance signals (BRDF), potentially leading to an
644 underestimation of AOD due to misattribution of aerosol contributions to surface reflectance.
645 In contrast, when dust loading is dominated by coarse and non-spherical particles (in May),
646 MISR demonstrates relatively better performance than MODIS (as shown by scatter plots).
647 This difference may be attributed to the advantage of MISR’s multi-angle observation
648 capability, consistent with findings from Middle Eastern validation studies (Farahat, 2019;
649 Garay et al., 2017).

650 **Table 1:** Number of ground stations data used in different months of the year 2012, 2016, and
651 2021.

| 2012 | 2016 | 2021 | 2012 | 2016 | 2021 | 2012 | 2016 | 2021 |
|------|------|------|------|------|------|------|------|------|
| Jan | Jan | Jan | May | May | May | Nov | Nov | Nov |
| 21 | 26 | 16 | 22 | 25 | 13 | 27 | 26 | 16 |

652 3.3 Fusion of satellite- and ground-based AOD

653 3.3.1 Variogram analysis

654 For the fusion of satellite- and ground-based AOD, the experimental variogram (using eq.2) is
655 first obtained from the gridded satellite data. As mentioned in section 2.3.2, a well-fitted
656 variogram is essential for determining appropriate parameters in geographical processes.
657 These variogram parameters like sill, range, and nugget are not unique but depend on the
658 theoretical models used. The choice of fitting is determined through a least square approach,
659 selecting the best fit based on the least sum of squared errors (SSE). However, the availability
660 of a large number of satellite data sets has made this task easier. The variogram depicted in
661 supplementary **Figs. S14, S15, and S16** demonstrate a flattening of variance after a certain
662 lag (interval between distances), affirming the effectiveness of our implemented detrending
663 method. AOD values within the range highlight spatial correlation, wherein the correlated
664 AOD values are influential in determining missing AOD values. The variogram parameters
665 obtained from the fitted theoretical model are given in **Tables 2 and 3**.

666 The variogram parameters corresponding to different sensors exhibit noticeable variation
667 across months and years, reflecting differences in their retrieval characteristics and ability to
668 represent AOD. For instance, both MODIS and MISR show shorter spatial correlation lengths
669 in May compared to January and November. Such reduced ranges are typically associated
670 with long-range dust or smoke transport processes, which dominate during this period in the
671 study region. Conversely, longer ranges indicate that the sensor retrievals capture more
672 spatially homogeneous values, suggesting an improved ability to represent regional
673 heterogeneity. In this study, we prioritize MODIS variograms because of their higher sill and
674 range values, which demonstrate stronger spatial dependency (Isaaks, 1991; Vieira et al.,
675 2009). Nevertheless, sensitivity tests indicate that using variograms derived from either
676 MODIS or MISR produces only negligible differences (~ 0.01) in the fused AOD estimates.
677 (**Fig. S17**). At this stage, it is also to be noted that geographically weighted or local variogram

678 approaches can better represent spatial heterogeneity, particularly over complex terrains such
679 as the Himalayas and Western Ghats. However, in the present study, this approach was not
680 feasible due to the limited availability of ground-based AOD observations, especially across
681 high-altitude regions. The sparse coverage restricts the stability and generalizability of local
682 variogram fitting, particularly at regional boundaries where different models would be
683 required. For this reason, we adopted a single variogram model, following the approach used
684 for large regions (e.g., eastern and western USA; Chatterjee et al. (2010)), which provides a
685 more consistent framework for regional-scale fusion).

686 **Table 2:** Parameters obtained from variogram in different seasons (January, May, and
687 November) of different years (2012, 2016, and 2021) from MODIS.

| Year | Month | MODEL | Nugget | sill | Range (in km) |
|------|-------|-------------|----------|----------|---------------|
| 2012 | Jan | Matheron | 0 | 0.033954 | 848.5 |
| 2016 | Jan | Exponential | 0.000015 | 0.057399 | 453.3 |
| 2021 | Jan | Exponential | 0 | 0.052327 | 854.0 |
| 2012 | May | Matheron | 0 | 0.026499 | 555.6 |
| 2016 | May | Matheron | 0 | 0.029704 | 489.1 |
| 2021 | May | Matheron | 0 | 0.034273 | 378.3 |
| 2012 | Nov | Matheron | 0 | 0.030027 | 548.3 |
| 2016 | Nov | Spherical | 0 | 0.029582 | 1080.7 |
| 2021 | Nov | Exponential | 0 | 0.040153 | 696.2 |

688 **Table 3:** Parameters obtained from variogram in different seasons (January, May, and
689 November) of different years (2012, 2016, and 2021) from MISR.

| Year | Month | MODEL | Nugget | sill | Range (in km) |
|------|-------|-------------|-----------|----------|---------------|
| 2012 | Jan | Exponential | 0.000062 | 0.011589 | 645.6 |
| 2016 | Jan | Spherical | 0.000177 | 0.017749 | 1060.6 |
| 2021 | Jan | Matheron | 0 | 0.027958 | 927.9 |
| 2012 | May | Matheron | 0 | 0.016100 | 371.1 |
| 2016 | May | Exponential | 0.001741 | 0.018171 | 463.0 |
| 2021 | May | Matheron | 0.000833 | 0.017896 | 533.5 |
| 2012 | Nov | Exponential | 0.000022 | 0.014509 | 638.7 |
| 2016 | Nov | Matheron | 0 | 0.018378 | 583.0 |
| 2021 | Nov | Matheron | 0.0000925 | 0.019104 | 516.4 |

690 3.3.2 Spatial interpolation of AOD

691 Monthly mean AOD gives the advantage of having full regional picture of columnar aerosol
692 load over south-Asian region. However, it is observed that both MODIS and MISR AOD
693 show gaps in some of the regions, either due to consistent cloud coverage or due to complex
694 orography coupled with highly reflective land masses (e.g., snow-covered regions of the
695 Himalayas). Hence, UK with geographic parameters as regressors applied to fill these missing
696 areas (which are found to be $\sim 2-11\%$) to obtain a complete spatial picture of AOD over the
697 south-Asian region. Since kriging gives a probability map, the associated variance is higher in

698 the gap regions than in the regions where values exist. Thus, the interpolated values and
699 variances are not unique, as they depend on the variogram and trend models used in the
700 interpolation. On the other hand, the variogram can have uncertainties that stem from factors
701 such as lag spacing, the quantity of data points, and model fitting, as highlighted by
702 researchers (Derakhshan and Leuangthong, 1982; Koushavand and Deutsch, 2008). Hence,
703 our proposed approach is not intended solely to enhance spatial coverage, but to generate a
704 bias-corrected and internally consistent AOD dataset through the optimal integration of
705 complementary satellite products.

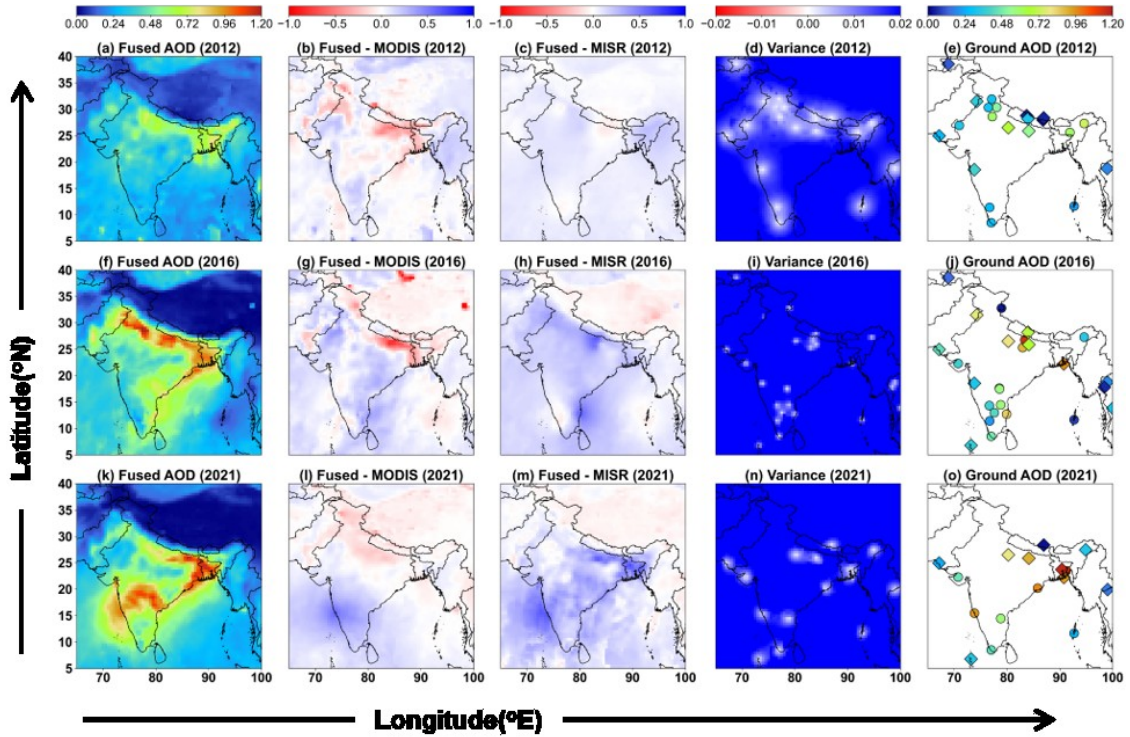
706 The spatial distribution of 0.5° gridded monthly mean raw and predicted (after spatial
707 interpolation) AOD from MODIS and MISR is shown in supplementary **Figs. S18-S23**. The
708 performance metrics (in terms of R and RMSE) of this gap-filling approach are demonstrated
709 through sensitivity studies, considering different spatial gaps in the data (**Fig. S24**). It is
710 observed that the predicted AOD largely depends on the availability and spatial distribution
711 of nearby observed data points. Regions such as the IGP, the Himalayan region, peninsular
712 India, and oceanic areas generally show better performance, where smoother spatial gradients
713 of AOD and more consistent regional aerosol patterns improve the reliability of the spatial
714 predictions. Based on these sensitivity studies, the predicted AOD field appears to provide a
715 reliable spatial representation with acceptable uncertainty as the interpolation (gap filling) is
716 made over a relatively small fraction of missing values based on a large number of observed
717 data points around the gap areas.

718 **3.3.3 Fused AOD**

719 The monthly fused AOD is generated using the UK fusion method, where satellite data are
720 treated as trend model. This retains the overall spatial signatures of AOD from each satellite
721 sensor. The optimal AOD values are determined by the weights obtained from spatial
722 relationships, along with the trend of the satellite-based AOD at the estimation locations.
723 **Figs. 4-6** show the fused maps of AOD at different seasons of the years 2012, 2016, and
724 2021. The regional average values of fused AOD, along with AOD from individual sensors,
725 are given in **Supplementary Tables ST4, ST5, and ST6**.

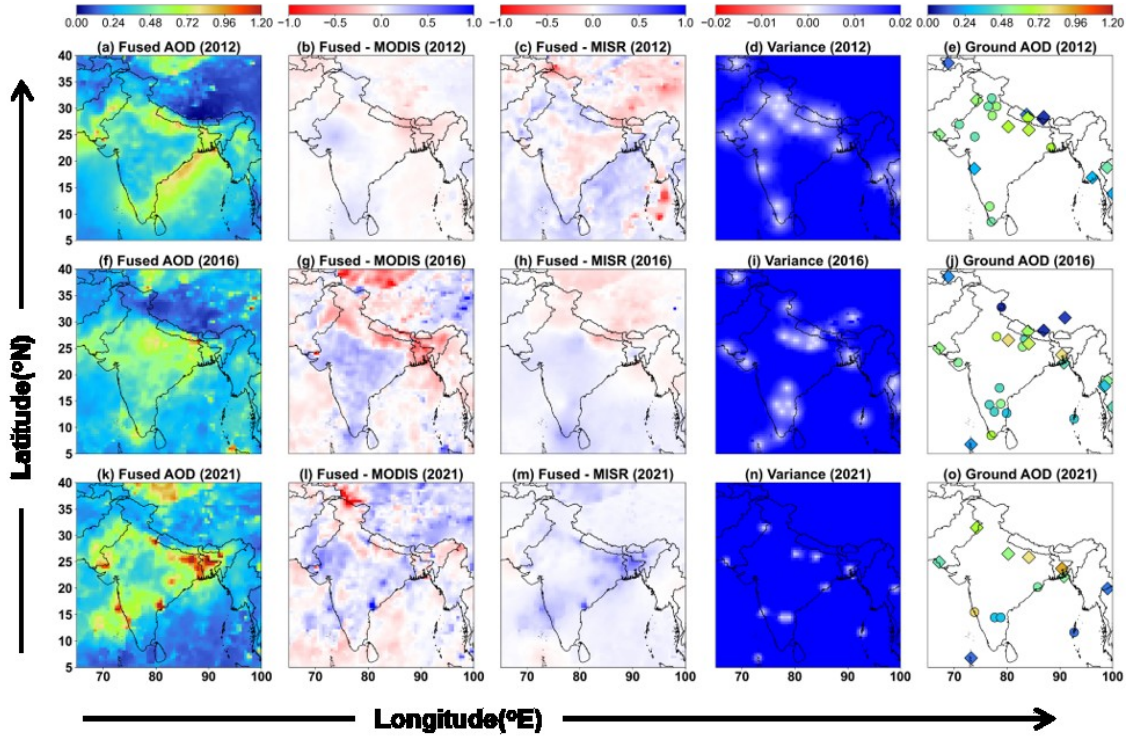
726 Throughout the observation period, the fusion maps highlight the significant influence of
727 ground-based AOD on the fusion method. As shown in **Table 4**, the fused AOD is more
728 aligned to ground-based AOD with a correlation (R) $\sim 0.994-1$ and RMSE $\sim 0.009-0.04$. On
729 the other hand, correlation between MODIS/MISR and fused AOD shows little improvement
730 compared to that between MODIS/MISR and ground-based AOD (**Table 5a, b**). This
731 indicates the robustness of the fusion approach keeping ground-based AOD as an anchoring
732 reference.

733 The notable outcomes from fused AOD maps are the distinct spatial features compared to
734 those obtained from individual space-based sensors. For example, during January 2016, the
735 significant overestimation by MODIS (AOD ~ 1.7) relative to ground-based AOD (~ 1.2) is
736 adjusted in the fused AOD distribution, thus correcting the bias but maintaining the spatial
737 heterogeneity. Similarly, in Jan 2021, MODIS and MISR significantly underestimated AOD
738 over peninsular India (MODIS AOD ~ 0.36 and MISR AOD ~ 0.30) as compared to ground
739 AOD (e.g., AOD at GOA ~ 0.95). The fused AOD corrects this bias toward values closer to
740 ground-based observations, retaining continuous flow of aerosols toward the Arabian coast.



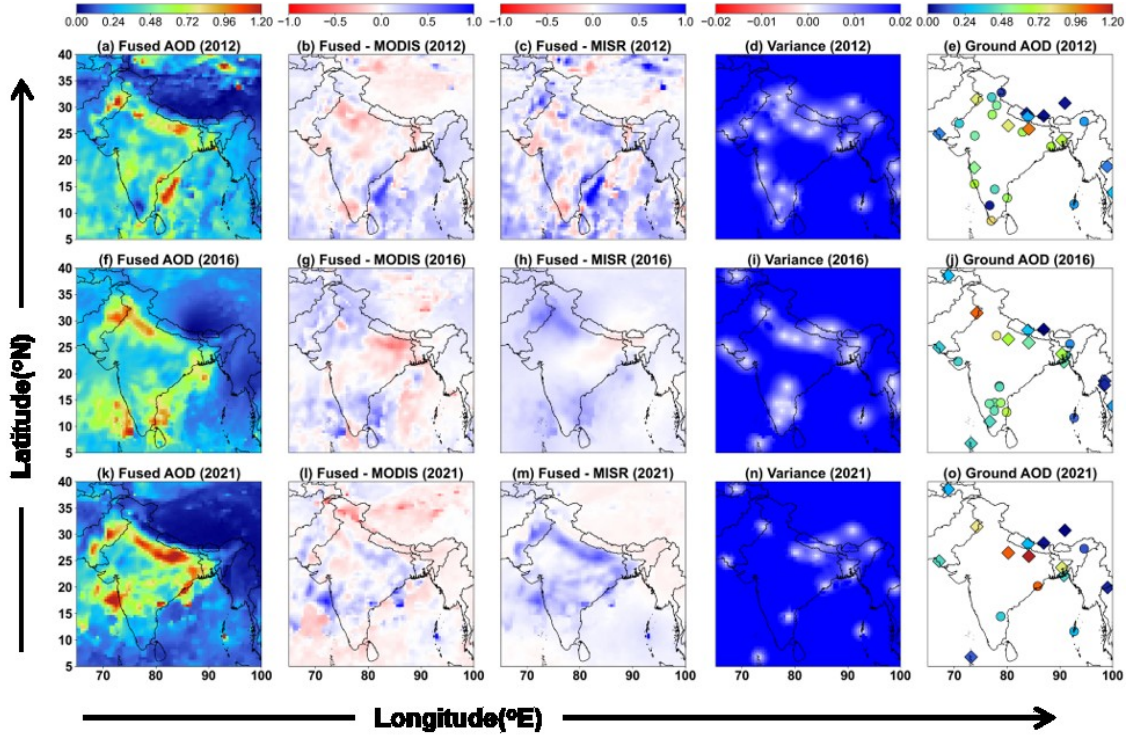
741

742 **Figure 4.** Monthly fused AOD (at 550 nm) maps [(a), (f) and (k)] in January for the years
 743 2012, 2016, 2021; [(b), (g) and (i)] and [(c), (h) and (m)] - the deviations of fused AOD from
 744 corresponding sensors, i.e., MODIS and MISR; [(d), (i) and (n)] variance; and [(e), (j) and
 745 (o)] - ground-based AOD (ARFINET is represented by circle and AERONET by diamond
 746 shapes) used to generate fused maps. Blue indicates overestimations, and red means an
 747 underestimation of fused AOD from satellite retrieved AOD. The white dots in variance plots
 748 show the ground station locations.



749

750 **Figure 5.** Similar analysis as in Fig. 4, but for the month of May in 2012, 2016, and 2021.



751

752 **Figure 6.** Similar analysis as in Fig. 4, but for the month of November in 2012, 2016, and
 753 2021.

754 **Table 4:** Comparative analysis of fused vs ground –based AOD at ground station locations.

| Year | Month | Fused & Ground | | | | |
|------|-------|----------------|-------|-------|-------|--------|
| | | Correlation | RMSE | MAE | Slope | Bias |
| 2012 | Jan | 0.998 | 0.014 | 0.011 | 1.024 | 0.003 |
| | May | 0.998 | 0.014 | 0.011 | 1.012 | 0.003 |
| | Nov | 0.996 | 0.025 | 0.017 | 1.026 | 0.004 |
| 2016 | Jan | 0.994 | 0.032 | 0.023 | 1.026 | -0.006 |
| | May | 0.984 | 0.04 | 0.026 | 1.074 | 0.004 |
| | Nov | 0.994 | 0.026 | 0.018 | 0.994 | -0.003 |
| 2021 | Jan | 0.999 | 0.022 | 0.015 | 1.03 | 0.008 |
| | May | 0.998 | 0.022 | 0.016 | 1.049 | 0.009 |
| | Nov | 1 | 0.009 | 0.007 | 1.003 | 0.002 |

755 Similar observations are also evident during the pre-monsoon period. However, during this
 756 period, the fused maps retain more of MISR spatial patterns in 2016 and 2021, while
 757 resembling MODIS in 2012. Notably, the discrepancies seen near coastal regions in May
 758 (2021), particularly across the peninsular zone, may be attributed to higher cloud fractions
 759 (**Fig. S25**), introducing greater uncertainty in aerosol-cloud discrimination (Lang et al., 2026),
 760 thereby leading to inaccuracies in satellite-derived AOD estimate. Furthermore, AOD
 761 retrievals in coastal areas may also be influenced by potential overestimation of boundary
 762 layer height (BLH) in MODIS data (Wang et al., 2025a). The fused AOD, which primarily
 763 incorporates the information from the availability and spatial proximity of ground-based
 764 measurements, tends to show higher values in these regions, effectively correcting this bias
 765 using ground-based observations.

766 **Table 5a:** Error and bias analysis of MODIS AOD with ground and fused AOD at ground
 767 station locations.

| Year | Month | MODIS & Ground | | | | | MODIS & Fused | | | | |
|------|-------|----------------|--------------|--------------|--------------|--------------|---------------|--------------|--------------|--------------|---------------|
| | | Correlation | RMSE | MAE | Slope | Bias | Correlation | RMSE | MAE | Slope | Bias |
| 2012 | Jan | 0.781 | 0.144 | 0.106 | 0.858 | 0.074 | 0.789 | 0.142 | 0.105 | 0.896 | 0.067 |
| | May | 0.770 | 0.128 | 0.102 | 0.704 | 0.147 | 0.788 | 0.122 | 0.096 | 0.732 | 0.137 |
| | Nov | 0.846 | 0.155 | 0.120 | 0.872 | 0.049 | 0.871 | 0.140 | 0.108 | 0.924 | 0.030 |
| 2016 | Jan | 0.792 | 0.250 | 0.164 | 1.096 | -0.037 | 0.822 | 0.237 | 0.154 | 1.175 | -0.083 |
| | May | 0.542 | 0.269 | 0.207 | 0.776 | 0.184 | 0.583 | 0.259 | 0.208 | 0.910 | 0.127 |
| | Nov | 0.773 | 0.157 | 0.121 | 0.759 | 0.064 | 0.787 | 0.153 | 0.115 | 0.774 | 0.055 |
| 2021 | Jan | 0.861 | 0.199 | 0.138 | 0.911 | 0.010 | 0.879 | 0.185 | 0.127 | 0.958 | -0.011 |
| | May | 0.752 | 0.236 | 0.152 | 1.030 | 0.038 | 0.778 | 0.230 | 0.147 | 1.120 | 0.004 |
| | Nov | 0.944 | 0.143 | 0.120 | 0.761 | 0.082 | 0.947 | 0.139 | 0.115 | 0.766 | 0.082 |

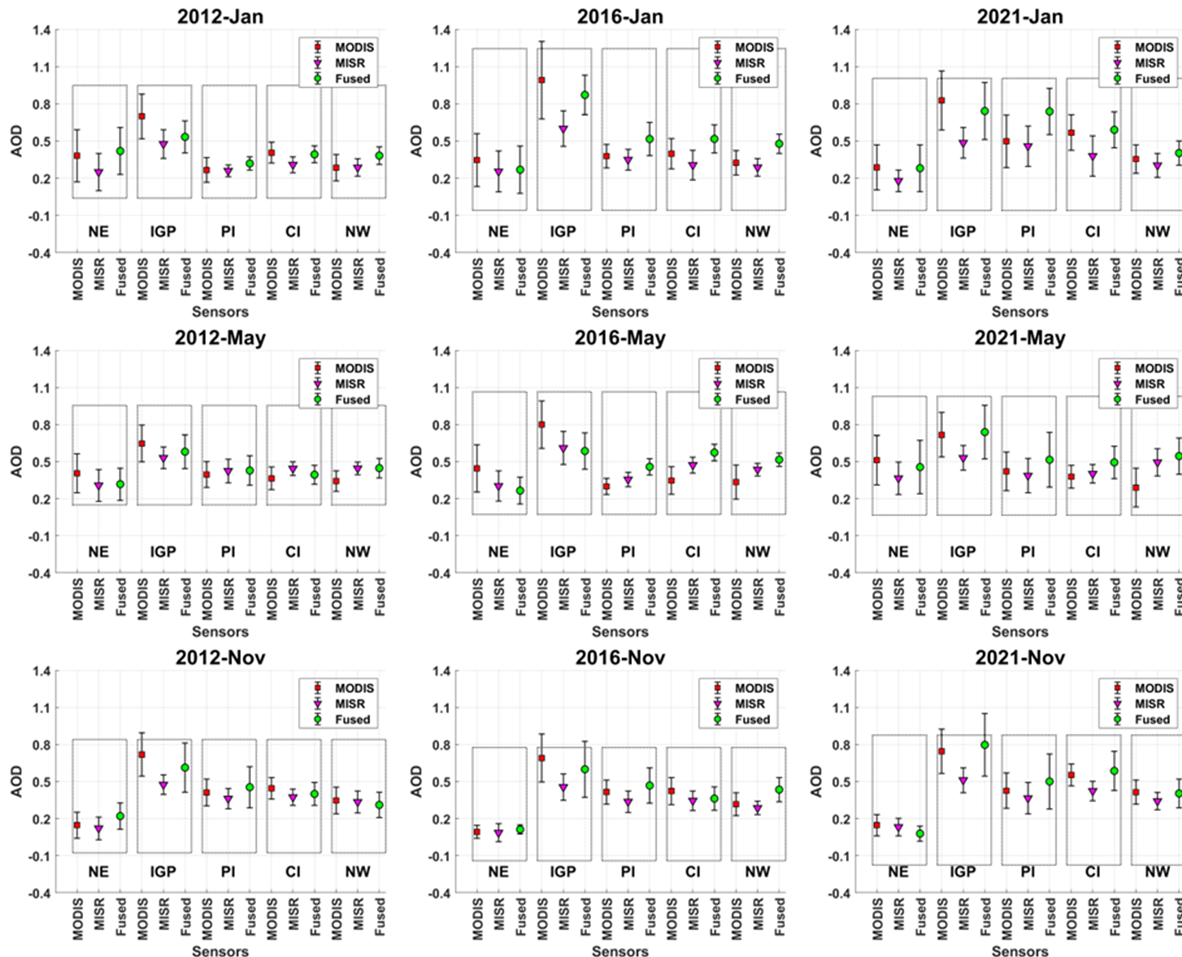
768 **Table 5b:** Error and bias analysis of MISR AOD with ground and fused AOD at ground
 769 station locations.

| Year | Month | MODIS & Ground | | | | | MODIS & Fused | | | | |
|------|-------|----------------|--------------|--------------|--------------|--------------|---------------|--------------|--------------|--------------|--------------|
| | | Correlation | RMSE | MAE | Slope | Bias | Correlation | RMSE | MAE | Slope | Bias |
| 2012 | Jan | 0.884 | 0.115 | 0.090 | 0.676 | 0.049 | 0.897 | 0.106 | 0.082 | 0.704 | 0.042 |
| | May | 0.643 | 0.159 | 0.132 | 0.437 | 0.189 | 0.656 | 0.154 | 0.129 | 0.452 | 0.184 |
| | Nov | 0.760 | 0.223 | 0.175 | 0.466 | 0.098 | 0.780 | 0.212 | 0.168 | 0.492 | 0.089 |
| 2016 | Jan | 0.783 | 0.270 | 0.206 | 0.421 | 0.010 | 0.818 | 0.263 | 0.203 | 0.454 | 0.081 |
| | May | 0.662 | 0.167 | 0.129 | 0.606 | 0.153 | 0.736 | 0.140 | 0.117 | 0.736 | 0.098 |
| | Nov | 0.814 | 0.186 | 0.143 | 0.515 | 0.079 | 0.834 | 0.185 | 0.144 | 0.528 | 0.072 |
| 2021 | Jan | 0.824 | 0.346 | 0.267 | 0.372 | 0.131 | 0.838 | 0.332 | 0.258 | 0.390 | 0.123 |
| | May | 0.772 | 0.205 | 0.160 | 0.458 | 0.147 | 0.805 | 0.185 | 0.147 | 0.502 | 0.130 |
| | Nov | 0.944 | 0.251 | 0.186 | 0.492 | 0.092 | 0.948 | 0.248 | 0.182 | 0.495 | 0.091 |

770 During the retreating monsoon season, the association of satellite and ground AOD is good,
 771 with similar spatial distribution over northern regions, while significant differences exists
 772 over southern parts. In the spatial map of fused AOD, the bias correction is clearly seen. In
 773 November 2016, over the NW and IGP, a significant bias correction in satellite AOD is
 774 observed, which is clearly indicated by the observed difference between fused AOD and
 775 satellite measurements. Similarly, a flow pattern on the east coast of peninsular India is
 776 corrected by fused AOD, which was otherwise underestimated by MISR (though retaining the
 777 spatial pattern). Here, the fused map showed enhanced AOD attributed to observations from
 778 ground stations, viz. Chennai (CHN) and Kadapa (KDP), which were underestimated by both
 779 MODIS and MISR. Similarly, in November 2021, the flow over the IGP is modified in the
 780 fused map based on ground observations

781 Over the IGP, where ground-based observations are more abundant than in other regions of
 782 India, the regional mean fused AOD generally lies between MODIS and MISR values. This
 783 reflects that the fusion process balances the biases between the tendency of MODIS to
 784 overestimate and MISR to underestimate AOD in this region. In contrast, over Peninsular
 785 India, which has the second-highest number of ground stations after the IGP, the fused AOD
 786 is higher than both MODIS and MISR, suggesting that satellite based underestimation is
 787 further adjusted in this region. Over northwest India during May, when dust loading is high,
 788 the fused AOD is closer to MISR, consistent with previous studies showing that MISR
 789 performs better than MODIS in dust-dominated regions due to its multi-angle capability.
 790 However, over the NE, CI, and NW regions, the fused AOD remains higher than satellite

791 estimates. Fused AOD estimates over the Himalayas and oceanic regions are not analyzed in
 792 detail due to the lack of sufficiently distributed ground-based observations. Overall, the fused
 793 AOD is constrained locally on ground-based AOD, which are generally considered more
 794 accurate than satellite-based observations whereas satellite retrievals exhibit discrepancies
 795 due to variations in aerosol types and their source contributions, which likely explain the
 796 observed differences in AOD estimates (Li et al., 2025; Wang et al., 2025b).



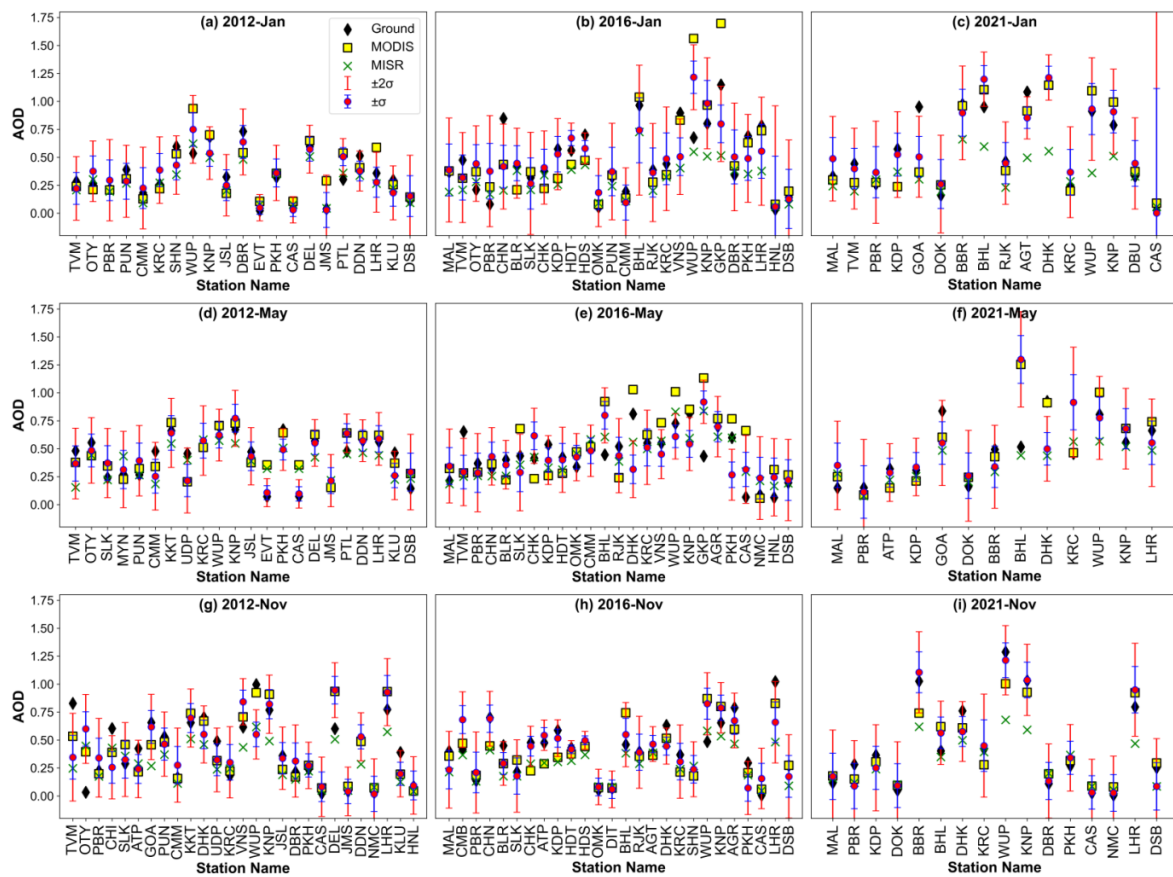
797
 798 **Figure 7.** The regional mean values of MODIS, MISR, and fused AOD. On the y-axis, AOD
 799 values are shown as mean \pm standard deviation.

800 With a view to assessing the improvement in the fused AOD estimates over MODIS and
 801 MISR, further analysis is carried out on regional scale considering different sub-regions over
 802 the study domain. **Fig. 7** shows the regional mean values of fused AOD along with AOD
 803 from individual satellite sensors. It is observed that the fused AOD significantly improves the
 804 biases in AOD from individual sensors. For example, in January 2012, MODIS AOD was
 805 significantly higher than fused AOD over IGP, while MISR AOD was closer to fused AOD
 806 over NE and CI regions. This indicates that the overestimation by MODIS in the IGP and the
 807 underestimation by MISR in the NE and CI regions are effectively corrected by the fusion
 808 framework. Similarly, in 2016, MODIS significantly overestimated AOD ($\sim 0.99 \pm 0.31$) in
 809 the IGP region. However, this was corrected in the fused AOD $\sim 0.87 \pm 0.16$, which also
 810 closely matches ground-based AOD (~ 0.86). During the pre-monsoon period, MISR AOD
 811 during 2012 and 2016 is closer to fused AOD; whereas in 2021, MODIS is closer to the fused
 812 AOD over the NE, IGP, and PI regions than MISR, except over the CI and NW regions. This

813 behavior is consistent with the lower RMSE of MISR relative to ground-based AOD. Post-
 814 monsoon analysis reveals MODIS AOD is closer to fused AOD over IGP with an
 815 overestimation in 2012 and 2016, and an opposite pattern in 2021. MISR AOD is lower than
 816 fused AOD in all these periods. These observations clearly indicate the regional level bias
 817 corrections in the individual satellite sensors, resulting in a more accurate representation of
 818 aerosol features in terms of fused AOD.

819 3.3.4 Performance analysis and cross-validation

820 The performance analysis carried out using the correlation analysis parameters such as RMSE
 821 and MAE, revealed a decrease in RMSE and MAE in fused data and an increase in
 822 correlation with MODIS and MISR (Figs S26-S28; Table 4, 5). However, the improvement
 823 is inconsistent due to factors such as the variogram model used, errors between observation
 824 values of ground observation, and MODIS, MISR. Thus, the final characteristics of fused
 825 products are influenced by their individual instruments. The accuracy of fusion can be
 826 concluded from the cross-validation analysis. This is characterized by LOOCV method.



827
 828 **Figure 8.** Predicted AOD values (as magenta points) with error bars $\pm\sigma$ (blue line), $\pm 2\sigma$ (red
 829 line), and ground observed AOD (black diamond), MODIS observation (yellow square),
 830 MISR (green cross) at different stations. For station names refer **Table ST7 and ST8**.

831 **Figure 8** shows the predicted AOD values at each ground location during each leave-one-out
 832 process. The prediction model performances analyzed in terms of mean prediction error
 833 (MPE) and root mean square prediction error (RMSPE) are given in **Table 6**. The predicted
 834 AOD values (as magenta points) at each of the ground locations with standard error bars $\pm \sigma$
 835 (blue line), $\pm 2\sigma$ (grey line) are also shown in **Fig. 8**, along with AOD from the ground (black
 836 diamond), MODIS (yellow triangle), MISR (red cross) observations. The figure shows that

837 more than 80% of ground AOD are within $\pm 2\sigma$ (95% Confidence interval) of predicted AOD
 838 for seven out of nine months. The highest accuracy was achieved in 2021 November and
 839 2012 May (100%), and the lowest in 2016 May (76%), indicating the importance of the
 840 association between different sensors during the fusion process. The enhanced accuracy of the
 841 model for fused estimations required good correlation and reduced errors, as indicated in
 842 **Tables 4, 5 & 6.**

843 **Table 6:** Accuracy assessment of the predicted AOD through leave-one-out cross-validation.
 844 Here % describes how many ground AOD (actual values) are covered within the range of
 845 predicted AOD.

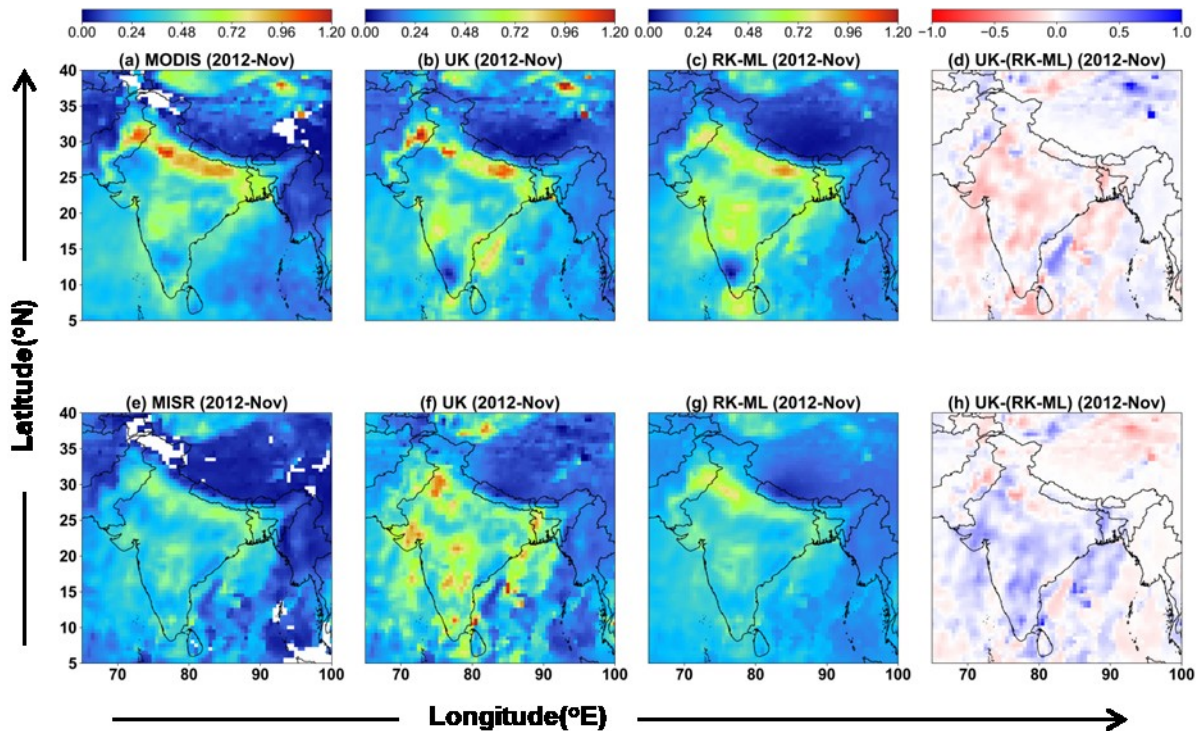
| Year | Month | Correlation | RMSPE | MPE | Ground AOD within $\pm\sigma$ (in %) | Ground AOD within $\pm 2\sigma$ (in %) |
|------|-------|--------------|--------------|--------------|---|---|
| 2012 | Jan | 0.852 | 0.108 | 0.091 | 76.19 | 95.24 |
| | May | 0.809 | 0.118 | 0.093 | 77.27 | 100 |
| | Nov | 0.676 | 0.215 | 0.152 | 59.26 | 77.78 |
| 2016 | Jan | 0.708 | 0.213 | 0.160 | 65.38 | 84.62 |
| | May | 0.367 | 0.219 | 0.170 | 56 | 76 |
| | Nov | 0.793 | 0.146 | 0.109 | 65.38 | 88.46 |
| 2021 | Jan | 0.893 | 0.162 | 0.121 | 81.25 | 81.25 |
| | May | 0.451 | 0.302 | 0.212 | 61.54 | 84.62 |
| | Nov | 0.964 | 0.108 | 0.086 | 87.50 | 100 |

846 3.3.5 Machine Learning enhanced Geostatistical data fusion

847 To understand the influence of number of ground measurement points in the generation of
 848 fused map, sensitivity studies has been carried out by varying the number of ground based
 849 measurement points. The number of ground points from maximum of 27 ground locations has
 850 been subsequently reduced to 22, 13, 8, and 6 respectively. The corresponding variations in
 851 the fused outputs are provided (Supplementary **Fig. S29-S30, Table ST9**) and a special case
 852 is included in **Fig. 9**. The figure clearly explains the changes in prevailing spatial pattern of
 853 aerosols according to changes in number of data points, indicating that RK-ML method is a
 854 good alternative to UK, when the available ground measurements are limited. This study also
 855 indicates an inherent limitation in UK method, alike to multiple linear regression models,
 856 which are highly susceptible to noise in predictor variables. In contrast, RK-ML demonstrates
 857 greater robustness by first modeling the deterministic component using a machine learning
 858 regressor (in this case, SVR), followed by kriging of the residuals to capture the stochastic
 859 component. This two-step approach effectively leverages machine learning for optimized
 860 estimation under noisy conditions, while kriging incorporates spatial variability of residuals
 861 obtained from observations, resulting in more reliable spatial predictions.

862 Notably, when data points are fewer, UK has overestimated AOD values in mainland regions
 863 relative to RK-ML predictions. This discrepancy may arise due to the complexity of the
 864 underlying surface, where OK has been shown to outperform UK, as discussed on basis of
 865 different surface types (Zimmerman et al., 1999). Since RK is an extension of OK, it inherits
 866 these advantages, contributing to the improved performance of the RK-ML method. The
 867 sensitivity study further highlights that variations in the number of ground station data points
 868 and associated errors have a lesser impact on fused AOD from RK-ML approach in terms of
 869 retaining spatial patterns compared to the UK-approach. This demonstrates the RK-ML
 870 fusion ability to better manage observational uncertainties and data sparsely.

871

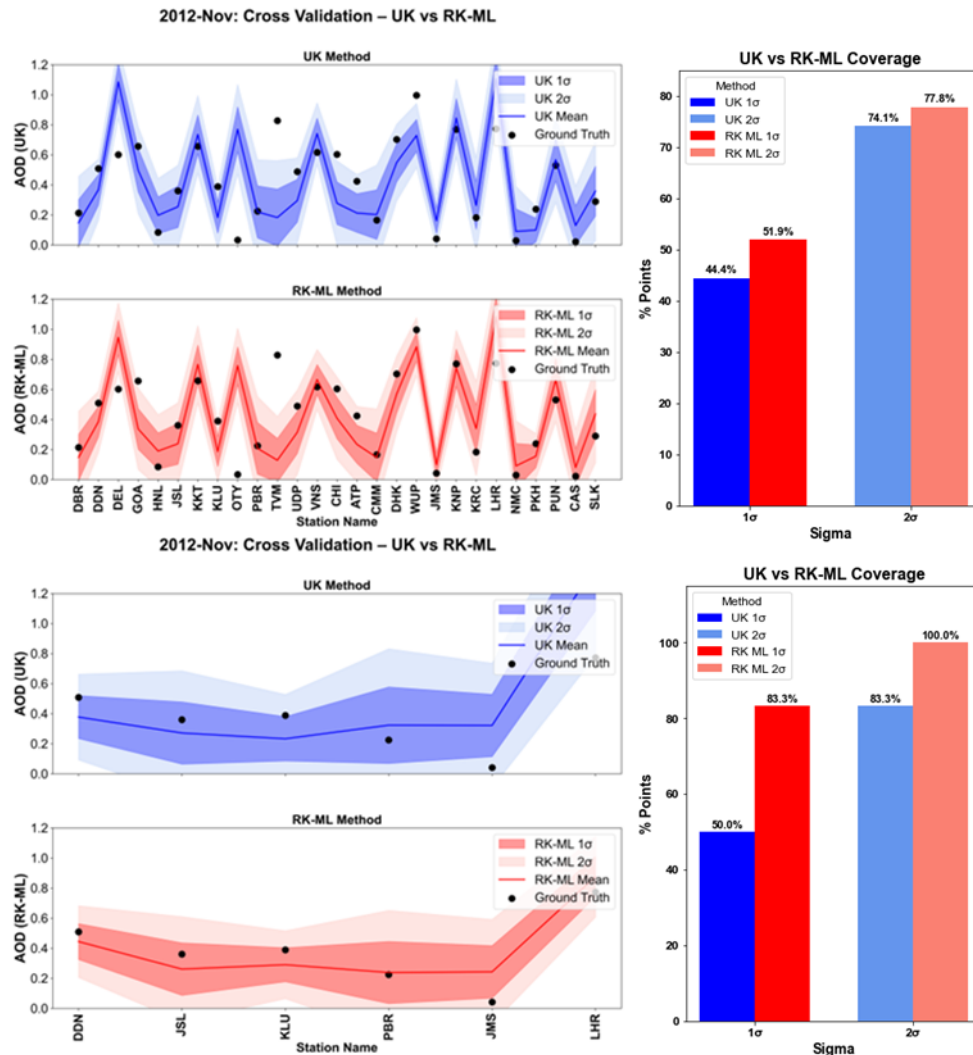


872
 873 **Figure 9.** MODIS (a), MISR (e), and fused AOD using Universal Kriging (UK, (b), (f)), and
 874 Residual Kriging with Machine Learning (RK-ML, (c), (g)); Difference between UK and RK-
 875 ML predictions ((d), (h)). Blue color in difference map indicates where UK predictions
 876 exceed those of RK-ML, and vice versa for red. The top panels (b, c and d) of fused AOD
 877 shows estimations using 27 ground-data points (Case - 1), while the bottom panel (f, g and h)
 878 shows fused AOD derived from 6 ground-data points (Case - 2).

879 The UK and RK-ML approach yields comparable results when the observations are higher in
 880 number. On the other hand, RK-ML outperforms UK when the number of ground observation
 881 is significantly decreased (**Fig. 10**). Hence, the accuracy of this estimation is significantly
 882 influenced by the availability of small datasets, which indicates that the large number of
 883 ground stations are crucial for best representation of fused AOD products from Universal
 884 Kriging, while RK-ML is a good choice in case of limited number of ground observations.
 885 Hence, the applicability of RK-ML can be made for generating fused AOD on daily basis per
 886 each satellite overpasses over ground based stations.

887 The applicability of UK and RK-ML depends on their ability to capture realistic spatial
 888 patterns from spatially representative data points (e.g., ground-based AOD) in order to
 889 produce accurate fused AOD distributions. These estimations inherently carry uncertainties,
 890 which increase with distance from ground observation sites. Consequently, the resulting maps
 891 show elevated uncertainties in areas with sparse ground coverage. To evaluate model
 892 performance under varying ground-station availability, we employed LOOCV. Results
 893 indicate that RK-ML is generally more effective than UK when fewer ground observations
 894 are available, as it can capture nonlinear relationships and penalize erroneous AOD values.
 895 However, the Kriging step still requires a sufficient number of data points to propagate spatial
 896 residuals. Similarly, UK applied with a limited number of stations (e.g., 27 in the present
 897 study) estimates weights from collocated AOD points and satellite regressors (MODIS and
 898 MISR). Thus, accurate uncertainty representation and improved fused AOD maps require a
 899 more uniformly distributed network of ground stations. As illustrated in **Fig. S29**, increasing

900 station density enhances the similarity between fusion maps from both methods, as seen in the
 901 larger white patches of the deviation plots (Fig. S29 a-d).



902
 903 **Figure 10:** Line plots of LOOCV results from UK method (blue line) and RK-ML method
 904 (red line), covering the ground AOD (black dots) for Case - 1 (27 points, 1st and 2nd line
 905 plots) and case - 2 (6 points, 3rd and 4th line plots) within 1σ (dark shade) and 2σ (light
 906 shade). For station names and details, refer to supplementary **Table ST8 and ST9**.

907 4. Conclusion

908 The utilization of a universal Kriging approach, combining satellite-based measurements with
 909 ground-based observations, has demonstrated enhanced AOD estimation with reduced
 910 uncertainties compared to relying on a single instrument. Despite inherent differences among
 911 instruments, the implemented approach capitalizes on their complementary features,
 912 statistically combining the three datasets to provide robust estimates. The significant
 913 outcomes of this study are as follows:

- 914 • MODIS and MISR observations exhibit good but variable associations with ground-
 915 based AOD measurements influenced by seasonal and geographic differences.
- 916 • Variogram analysis reveals different autocorrelation length implying capability of
 917 each sensor to get the spatial variability or auto correlation structure in different
 918 periods. In some of the months, MODIS shows higher spatial range as compared to

919 MISR, while the opposite is seen during the rest of the months. On the other hand, sill
920 is always higher in case of MODIS.

- 921 • Spatial interpolation of AOD through variogram analysis provides very good
922 predictions at the missing grids of the satellite observations, emphasizing the
923 effectiveness of the universal Kriging method.
- 924 • The fused AOD maps reveal distinct results, highlighting the significant impact of
925 ground-based AOD on the fusion process. During the pre-monsoon period
926 specifically, the correlation coefficient and slope between MISR and fused AOD,
927 which is comparable to ground-based AOD at point locations, improved by ~11% and
928 ~21%, respectively. Furthermore, the RMSE was reduced by ~16% compared to pre-
929 fusion values. These results demonstrate a marked improvement in the spatial
930 representation of ground AOD following the fusion process. Additionally, the near-
931 perfect correlation ($R \sim 0.99$) between fused and ground-based AOD suggests effective
932 bias correction in MODIS or MISR datasets, which otherwise significantly
933 overestimated or underestimated aerosol measurements across certain parts of the
934 study region.
- 935 • Cross-validation experiments further underline the effectiveness of the models in this
936 study, e.g., strong correlations (0.964) and low RMSPE (0.108) and MPE (0.086)
937 errors during November 2021. Even the model is able to predict 87.50 % of ground
938 truths within $\pm\sigma$ and even 100% within $\pm 2\sigma$. Moreover the measurements which were
939 failed in predictions are due to highly local heterogeneity influenced by nearby ground
940 measurements only.
- 941 • Incorporating a greater number of ground-based measurements enhances the fused
942 results, yielding a cross-validation accuracy ranging from approximately 78% to 88%
943 (based on 27 ground location points in November 2012 and 26 points in November
944 2016). However, the alternative RK-ML method can also be effective when long-term
945 observation stations are available, even if their numbers are limited. The establishment
946 of additional ground-based stations is recommended to strengthen the representation
947 of air quality, especially in regions with high heterogeneity. This methodology can be
948 implemented to get the fusion maps of finer spatiotemporal resolution.

949 **Author Contributions Statement:**

950 **SSG** - Data Curation, Software, Formal analysis, Visualization, Investigation, Writing -
951 Original Draft and Editing; **MMG** - Methodology, Visualization, Validation, Software,
952 Writing, Review and Editing, Supervision; **SSB** - Conceptualization, Supervision, Review
953 and Editing, Project administration.

954 **Data availability:** ARFINET data used for this study are available upon request from
955 Surendran Nair Suresh Babu (s_sureshabu@vssc.gov.in). All other datasets used in this
956 paper are open access data, and can be freely downloaded from the websites listed in the
957 acknowledgements.

958 **Competing interests:** The contact author has declared that none of the authors has any
959 competing interests.

960

961

962 **Acknowledgements:**

963 This study was carried out as part of the ARFI project of ISRO-GBP. We express our sincere
964 thanks to the ARFINET investigators for the continued support and long-term contributions
965 over the years in operating the network. We authors are also thankful to the AERONET team
966 for providing AOD data (data available at <http://aeronet.gsfc.nasa.gov>). Additionally, we
967 acknowledge NASA's Level-1 and Atmosphere Archive and Distribution System Distributed
968 Active Archive Center (LAADS DAAC; data available at
969 https://ladsweb.modaps.eosdis.nasa.gov/archive/allData/61/MOD04_L2/) and the
970 Atmospheric Science Data Center (ASDC; data available at [https://10dup05.larc.nasa.gov/cgi-
971 bin/MISR/main.cgi](https://10dup05.larc.nasa.gov/cgi-bin/MISR/main.cgi)) for making the MODIS and MISR datasets available.

972 **References:**

- 973 Babu, S. S., Krishna Moorthy, K., and Satheesh, S. K.: Temporal heterogeneity in aerosol
974 characteristics and the resulting radiative impacts at a tropical coastal station – Part 2: Direct
975 short wave radiative forcing, *Ann. Geophys.*, 25, 2309–2320, [https://doi.org/10.5194/angeo-
976 25-2309-2007](https://doi.org/10.5194/angeo-25-2309-2007), 2007.
- 977 Bai, K., Li, K., Shao, L., Li, X., Liu, C., Li, Z., and Ma, M.: LGHAP v2 : a global gap-free
978 aerosol optical depth and PM_{2.5} concentration dataset since 2000 derived via big Earth data
979 analytics, 2425–2448, 2024.
- 980 Baisad, K., Chutsagulprom, N., and Moonchai, S.: A Non-Linear Trend Function for Kriging
981 with External Drift Using Least Squares Support Vector Regression, *Mathematics*, 11, 4799,
982 <https://doi.org/10.3390/math11234799>, 2023.
- 983 Basart, S., Pérez, C., Cuevas, E., Baldasano, J. M., and Gobbi, G. P.: Aerosol characterization
984 in Northern Africa, Northeastern Atlantic, mediterranean basin and middle east from direct-
985 sun AERONET observations, *Atmos. Chem. Phys.*, 9, 8265–8282,
986 <https://doi.org/10.5194/acp-9-8265-2009>, 2009.
- 987 Brereton, R. G. and Lloyd, G. R.: Support Vector Machines for classification and regression,
988 *Analyst*, 135, 230–267, <https://doi.org/10.1039/b918972f>, 2010.
- 989 Chatterjee, A., Michalak, A. M., Kahn, R. A., Paradise, S. R., Braverman, A. J., and Miller,
990 C. E.: A geostatistical data fusion technique for merging remote sensing and ground-based
991 observations of aerosol optical thickness, *J. Geophys. Res. Atmos.*, 115, 1–12,
992 <https://doi.org/10.1029/2009JD013765>, 2010.
- 993 Chen, Z.-Y., Jin, J.-Q., Zhang, R., Zhang, T.-H., Chen, J.-J., Yang, J., Ou, C.-Q., and Guo,
994 Y.: Comparison of Different Missing-Imputation Methods for MAIAC (Multiangle
995 Implementation of Atmospheric Correction) AOD in Estimating Daily PM_{2.5} Levels, *Remote
996 Sens.*, 12, <https://doi.org/10.3390/rs12183008>, 2020.
- 997 Chu, D. A., Kaufman, Y. J., Ichoku, C., Remer, L. A., Tanré, D., and Holben, B. N.:
998 Validation of MODIS aerosol optical depth retrieval over land, *Geophys. Res. Lett.*, 29,
999 MOD2-1-MOD2-4, <https://doi.org/10.1029/2001GL013205>, 2002.
- 1000 Chua, S. H. and Bras, R. L.: Optimal estimators of mean areal precipitation in regions of
1001 orographic influence, *J. Hydrol.*, 57, 23–48, [https://doi.org/10.1016/0022-1694\(82\)90101-9](https://doi.org/10.1016/0022-1694(82)90101-9),
1002 1982.
- 1003 Derakhshan, H. and Leuangthong, O.: Impact of Data Spacing on Variogram Uncertainty, 1–
1004 19, 1982.
- 1005 Eck, T. F., Holben, B. N., Reid, J. S., Dubovik, O., Smirnov, A., O’Neill, N. T., Slutsker, I.,
1006 and Kinne, S.: Wavelength dependence of the optical depth of biomass burning, urban, and
1007 desert dust aerosols, <https://doi.org/10.1029/1999JD900923>, 1999.
- 1008 Edward H. Isaaks, R. M. S.: An Introduction to Applied Geostatistics, *Comput. Geosci.*, 17,
1009 471–473, [https://doi.org/10.1016/0098-3004\(91\)90055-I](https://doi.org/10.1016/0098-3004(91)90055-I), 1991.
- 1010 Farahat, A.: Comparative analysis of MODIS, MISR, and AERONET climatology over the

1011 Middle East and North Africa, *Ann. Geophys.*, 37, 49–64, [https://doi.org/10.5194/angeo-37-](https://doi.org/10.5194/angeo-37-49-2019)
1012 49-2019, 2019.

1013 Filonchyk, M., Yan, H., Zhang, Z., Yang, S., Li, W., and Li, Y.: Combined use of satellite
1014 and surface observations to study aerosol optical depth in different regions of China, *Sci.*
1015 *Rep.*, 9, 1–15, <https://doi.org/10.1038/s41598-019-42466-6>, 2019.

1016 Freier, L. and Von Lieres, E.: Kriging based iterative parameter estimation procedure for
1017 biotechnology applications with nonlinear trend functions, *IFAC-PapersOnLine*, 28, 574–
1018 579, <https://doi.org/10.1016/j.ifacol.2015.05.043>, 2015.

1019 Freier, L., Wiechert, W., and von Lieres, E.: Kriging with trend functions nonlinear in their
1020 parameters: Theory and application in enzyme kinetics, *Eng. Life Sci.*, 17, 916–922,
1021 <https://doi.org/10.1002/elsc.201700022>, 2017.

1022 Gao, L., Chen, L., Li, C., Li, J., Che, H., and Zhang, Y.: Evaluation and possible uncertainty
1023 source analysis of JAXA Himawari-8 aerosol optical depth product over China, *Atmos. Res.*,
1024 248, 105248, <https://doi.org/10.1016/j.atmosres.2020.105248>, 2021.

1025 Garay, M. J., Kalashnikova, O. V., and Bull, M. A.: Development and assessment of a higher-
1026 spatial-resolution (4.4 km) MISR aerosol optical depth product using AERONET-DRAGON
1027 data, *Atmos. Chem. Phys.*, 17, 5095–5106, <https://doi.org/10.5194/acp-17-5095-2017>, 2017.

1028 Giles, D. M., Sinyuk, A., Sorokin, M. G., Schafer, J. S., Smirnov, A., Slutsker, I., Eck, T. F.,
1029 Holben, B. N., Lewis, J. R., Campbell, J. R., Welton, E. J., Korokin, S. V., and Lyapustin, A.
1030 I.: Advancements in the Aerosol Robotic Network (AERONET) Version 3 database -
1031 Automated near-real-time quality control algorithm with improved cloud screening for Sun
1032 photometer aerosol optical depth (AOD) measurements, *Atmos. Meas. Tech.*, 12, 169–209,
1033 <https://doi.org/10.5194/amt-12-169-2019>, 2019.

1034 Gogoi, M. M., Krishna Moorthy, K., Suresh Babu, S., and Bhuyan, P. K.: Climatology of
1035 columnar aerosol properties and the influence of synoptic conditions: First-time results from
1036 the northeastern region of India, *J. Geophys. Res. Atmos.*, 114,
1037 <https://doi.org/10.1029/2008JD010765>, 2009.

1038 Guo, J., Gu, X., Yu, T., Cheng, T., Chen, H., and Xie, D.: Trend analysis of the aerosol
1039 optical depth over China using fusion of MODIS and MISR aerosol products via adaptive
1040 weighted estimate algorithm, *Earth Obs. Syst. XVIII*, 8866, 88661X,
1041 <https://doi.org/10.1117/12.2024687>, 2013.

1042 Gupta, P., Patadia, F., and Christopher, S. A.: Multisensor data product fusion for aerosol
1043 research, *IEEE Trans. Geosci. Remote Sens.*, 46, 1407–1415,
1044 <https://doi.org/10.1109/TGRS.2008.916087>, 2008.

1045 Holben, B. N., Eck, T. F., Slutsker, I., Tanré, D., Buis, J. P., Setzer, A., Vermote, E., Reagan,
1046 J. A., Kaufman, Y. J., Nakajima, T., Lavenu, F., Jankowiak, I., and Smirnov, A.: AERONET
1047 - A federated instrument network and data archive for aerosol characterization, *Remote Sens.*
1048 *Environ.*, 66, 1–16, [https://doi.org/10.1016/S0034-4257\(98\)00031-5](https://doi.org/10.1016/S0034-4257(98)00031-5), 1998.

1049 Holdaway, M. R.: Spatial modeling and interpolation of monthly temperature using kriging,
1050 *Clim. Res.*, 6, 215–225, <https://doi.org/10.3354/cr006215>, 1996.

1051 Huang, J., Patrick Arnott, W., Barnard, J. C., and Holmes, H. A.: Theoretical uncertainty
1052 analysis of satellite retrieved aerosol optical depth associated with surface albedo and aerosol
1053 optical properties, *Remote Sens.*, 13, 1–21, <https://doi.org/10.3390/rs13030344>, 2021.

1054 Ichoku, C., Allen Chu, D., Mattoo, S., Kaufman, Y. J., Remer, L. A., Tanré, D., Slutsker, I.,
1055 and Holben, B. N.: A spatio-temporal approach for global validation and analysis of MODIS
1056 aerosol products, *Geophys. Res. Lett.*, 29, MOD1-1-MOD1-4,
1057 <https://doi.org/10.1029/2001GL013206>, 2002.

1058 Jiang, X., Liu, Y., Yu, B., and Jiang, M.: Comparison of MISR aerosol optical thickness with
1059 AERONET measurements in Beijing metropolitan area, *Remote Sens. Environ.*, 107, 45–53,
1060 <https://doi.org/10.1016/j.rse.2006.06.022>, 2007.

1061 Jiao, Y., Zhang, M., Wang, L., and Qin, W.: A New Cloud and Haze Mask Algorithm From

1062 Radiative Transfer Simulations Coupled With, *IEEE Trans. Geosci. Remote Sens.*, 61, 1–16,
1063 <https://doi.org/10.1109/TGRS.2023.3252264>, 2023.

1064 Jin, S., Ma, Y., Li, H., Liu, B., Fan, R., Zhang, M., Lopatin, A., Dubovik, O., Hu, X., Gong,
1065 W., and Wang, L.: Characterizing Aerosol Optical Properties and Direct Radiative Effects
1066 From the Perspective of Components : A Synergy Retrieval Study Based on Sun Photometer
1067 and Lidar in Central China, <https://doi.org/10.1029/2024GL113448>, 2025.

1068 Jinnagara Puttaswamy, S., Nguyen, H. M., Braverman, A., Hu, X., and Liu, Y.: Statistical
1069 data fusion of multi-sensor AOD over the Continental United States, *Geocarto Int.*, 29, 48–
1070 64, <https://doi.org/10.1080/10106049.2013.827750>, 2014.

1071 Kadow, C., Hall, D. M., and Ulbrich, U.: Artificial intelligence reconstructs missing climate
1072 information, *Nat. Geosci.*, 13, 408–413, <https://doi.org/10.1038/s41561-020-0582-5>, 2020.

1073 Kahn, R., Banerjee, P., and McDonald, D.: Sensitivity of multiangle imaging to natural
1074 mixtures of aerosols over ocean, *J. Geophys. Res. Atmos.*, 106, 18219–18238,
1075 <https://doi.org/10.1029/2000JD900497>, 2001.

1076 Kahn, R., Andrews, E., Brock, C. A., Chin, M., Feingold, G., Gettelman, A., Levy, R. C.,
1077 Murphy, D. M., Nenes, A., Pierce, J. R., Popp, T., Redemann, J., Sayer, A. M., da Silva, A.
1078 M., Sogacheva, L., and Stier, P.: Reducing Aerosol Forcing Uncertainty by Combining
1079 Models With Satellite and Within-The-Atmosphere Observations: A Three-Way Street, *Rev.*
1080 *Geophys.*, 61, 1–27, <https://doi.org/10.1029/2022rg000796>, 2023.

1081 Kalluri, R. O. R., Gugamsetty, B., Kotalo, R. G., Nagireddy, S. K. R., Tandule, C. R., Thotli,
1082 L. R., Rajuru Ramakrishna, R., and Surendranair, S. B.: Direct radiative forcing properties of
1083 atmospheric aerosols over semi-arid region, Anantapur in India, *Sci. Total Environ.*, 566–567,
1084 1002–1013, <https://doi.org/10.1016/j.scitotenv.2016.05.056>, 2016.

1085 Kim, M., Kim, J., Lim, H., Lee, S., Cho, Y., Lee, Y., Go, S., and Lee, K.: Aerosol optical
1086 depth data fusion with Geostationary Korea Multi-Purpose Satellite (GEO-KOMPSAT-2)
1087 instruments GEMS , AMI , and GOCI-II : statistical and deep neural network methods, 4317–
1088 4335, 2024.

1089 Kinne, S.: Remote sensing data combinations: superior global maps for aerosol optical depth,
1090 *Satell. Aerosol Remote Sens. over L.*, 361–381, [https://doi.org/10.1007/978-3-540-69397-](https://doi.org/10.1007/978-3-540-69397-0_12)
1091 [0_12](https://doi.org/10.1007/978-3-540-69397-0_12), 2009.

1092 Kompalli, S. K., Suresh Babu, S., and Krishna Moorthy, K.: Inter-comparison of aerosol
1093 optical depth from the Multi-Wavelength Solar Radiometer with other radiometric
1094 measurements, *Indian J. Radio Sp. Phys.*, 39, 364–371, 2010.

1095 Koushavand, B. and Deutsch, C. V: A Methodology to Quantify and Transfer Variogram
1096 Uncertainty through Kriging and Simulation, *Cent. Comput. Geostatistics*, 1–16, 2008.

1097 Kumar, K. R., Narasimhulu, K., Reddy, R. R., Gopal, K. R., Reddy, L. S. S., Balakrishnaiah,
1098 G., Moorthy, K. K., and Babu, S. S.: Temporal and spectral characteristics of aerosol optical
1099 depths in a semi-arid region of southern India, *Sci. Total Environ.*, 407, 2673–2688,
1100 <https://doi.org/10.1016/j.scitotenv.2008.10.028>, 2009.

1101 Kumar, S., Kumar, S., Singh, A. K., and Singh, R. P.: Seasonal variability of atmospheric
1102 aerosol over the North Indian region during 2005-2009, *Adv. Sp. Res.*, 50, 1220–1230,
1103 <https://doi.org/10.1016/j.asr.2012.06.022>, 2012.

1104 Lang, Q., Zhang, M., He, Q., Jin, S., Qin, W., Luo, L., and Wang, L.: Significant
1105 uncertainties from overlooking aerosol-cloud coexistence in surface solar radiation estimates
1106 using passive satellite observations, *Remote Sens. Environ.*, 333, 115168,
1107 <https://doi.org/https://doi.org/10.1016/j.rse.2025.115168>, 2026.

1108 Levy, R. C., Remer, L. A., Martins, J. V, Kaufman, Y. J., Plana-Fattori, A., Redemann, J.,
1109 and Wenny, B.: Evaluation of the MODIS Aerosol Retrievals over Ocean and Land during
1110 CLAMS, 2005.

1111 Li, H., Zhang, M., Wang, L., Su, X., and Lu, Y.: Effects of Different Types of Aerosols on
1112 Diffuse Radiation Based on Global AERONET, *J. Geophys. Res. Atmos.*, 130,

1113 e2024JD042701, <https://doi.org/https://doi.org/10.1029/2024JD042701>, 2025.

1114 Li, J., Kahn, R. A., Wei, J., Carlson, B. E., Lacis, A. A., Li, Z., Li, X., Dubovik, O., and
 1115 Nakajima, T.: Synergy of Satellite- and Ground-Based Aerosol Optical Depth Measurements
 1116 Using an Ensemble Kalman Filter Approach, *J. Geophys. Res. Atmos.*, 125, 1–17,
 1117 <https://doi.org/10.1029/2019JD031884>, 2020.

1118 Lilla, R. and Castrignanò, A.: Science of the Total Environment A geostatistical approach for
 1119 multi-source data fusion to predict water table depth Warning : Editor name is, *Sci. Total*
 1120 *Environ.*, 696, 133763, <https://doi.org/10.1016/j.scitotenv.2019.133763>, 2019.

1121 Litvinov, P., Chen, C., Dubovik, O., Zhai, S., Matar, C., Li, C., Lopatin, A., Fuertes, D.,
 1122 Lapyonok, T., Bindreiter, L., Dornacher, M., Lehner, A., Dandocsi, A., Gasbarra, D., and
 1123 Retscher, C.: Synergetic retrieval from multi-mission spaceborne measurements for enhanced
 1124 aerosol and surface characterization, 7679–7716, 2025.

1125 Liu, Y., Sarnat, J. A., Coull, B. A., Koutrakis, P., and Jacob, D. J.: Validation of Multiangle
 1126 Imaging Spectroradiometer (MISR) aerosol optical thickness measurements using Aerosol
 1127 Robotic Network (AERONET) observations over the contiguous United States, *J. Geophys.*
 1128 *Res. Atmos.*, 109, <https://doi.org/10.1029/2003jd003981>, 2004.

1129 Lodhi, N. K., Beegum, S. N., Singh, S., and Kumar, K.: Aerosol climatology at Delhi in the
 1130 western Indo-Gangetic Plain: Microphysics, long-term trends, and source strengths, *J.*
 1131 *Geophys. Res. Atmos.*, 118, 1361–1375, <https://doi.org/10.1002/jgrd.50165>, 2013.

1132 Moorthy, K. K., Babu, S. S., Satheesh, S. K., Srinivasan, J., and Dutt, C. B. S.: Dust
 1133 absorption over the “Great Indian Desert” inferred using ground-based and satellite remote
 1134 sensing, *J. Geophys. Res. Atmos.*, 112, 1–10, <https://doi.org/10.1029/2006JD007690>, 2007.

1135 Moorthy K., K., Suresh Babu, S., and Satheesh, S. K.: Temporal heterogeneity in aerosol
 1136 characteristics and the resulting radiative impact at a tropical coastal station – Part 1:
 1137 Microphysical and optical properties, *Ann. Geophys.*, 25, 2293–2308,
 1138 <https://doi.org/10.5194/angeo-25-2293-2007>, 2007.

1139 Nalder, I. A. and Wein, R. W.: Spatial interpolation of climatic Normals: Test of a new
 1140 method in the Canadian boreal forest, *Agric. For. Meteorol.*, 92, 211–225,
 1141 [https://doi.org/10.1016/S0168-1923\(98\)00102-6](https://doi.org/10.1016/S0168-1923(98)00102-6), 1998.

1142 Nguyen, H., Cressie, N., and Braverman, A.: Spatial statistical data fusion for remote sensing
 1143 applications, *J. Am. Stat. Assoc.*, 107, 1004–1018,
 1144 <https://doi.org/10.1080/01621459.2012.694717>, 2012.

1145 Nirala, M.: Multi-sensor data fusion of aerosol optical thickness, *Int. J. Remote Sens.*, 29,
 1146 2127–2136, <https://doi.org/10.1080/01431160701395336>, 2008.

1147 Pathak, H. S., Satheesh, S. K., Nanjundiah, R. S., Moorthy, K. K., Lakshmivarahan, S., and
 1148 Babu, S. N. S.: Assessment of regional aerosol radiative effects under the SWAAMI
 1149 campaign - Part 1: Quality-enhanced estimation of columnar aerosol extinction and
 1150 absorption over the Indian subcontinent, *Atmos. Chem. Phys.*, 19, 11865–11886,
 1151 <https://doi.org/10.5194/acp-19-11865-2019>, 2019.

1152 Prasad, A. K. and Singh, R. P.: Comparison of MISR-MODIS aerosol optical depth over the
 1153 Indo-Gangetic basin during the winter and summer seasons (2000-2005), *Remote Sens.*
 1154 *Environ.*, 107, 109–119, <https://doi.org/10.1016/j.rse.2006.09.026>, 2007.

1155 Rossi, R. E., Dungan, J. L., and Beck, L. R.: Kriging in the shadows: Geostatistical
 1156 interpolation for remote sensing, *Remote Sens. Environ.*, 49, 32–40,
 1157 [https://doi.org/10.1016/0034-4257\(94\)90057-4](https://doi.org/10.1016/0034-4257(94)90057-4), 1994.

1158 Sayer, A. M., Hsu, N. C., Bettenhausen, C., and Jeong, M. J.: Validation and uncertainty
 1159 estimates for MODIS Collection 6 “deep Blue” aerosol data, *J. Geophys. Res. Atmos.*, 118,
 1160 7864–7872, <https://doi.org/10.1002/jgrd.50600>, 2013.

1161 Sayer, A. M., Munchak, L. A., Hsu, N. C., Levy, R. C., Bettenhausen, C., and Jeong, M.-J.:
 1162 MODIS Collection 6 aerosol products: Comparison between Aqua’s e-Deep Blue, Dark
 1163 Target, and “merged” data sets, and usage recommendations, *J. Geophys. Res. Atmos.*, 119,

1164 13,913-965,989, <https://doi.org/https://doi.org/10.1002/2014JD022453>, 2014.

1165 Sayer, A. M., Govaerts, Y., Kolmonen, P., Lipponen, A., Luffarelli, M., Mielonen, T.,
1166 Patadia, F., Popp, T., Povey, A. C., Stebel, K., and Witek, M. L.: A review and framework for
1167 the evaluation of pixel-level uncertainty estimates in satellite aerosol remote sensing, *Atmos.*
1168 *Meas. Tech.*, 13, 373–404, <https://doi.org/10.5194/amt-13-373-2020>, 2020.

1169 Schutgens, N., Sayer, A. M., Heckel, A., Hsu, C., Jethva, H., De Leeuw, G., Leonard, P. J. T.,
1170 Levy, R. C., Lipponen, A., Lyapustin, A., North, P., Popp, T., Poulsen, C., Sawyer, V.,
1171 Sogacheva, L., Thomas, G., Torres, O., Wang, Y., Kinne, S., Schulz, M., Stier, P., and
1172 Schutgens, N.: An AeroCom-AeroSat study: Intercomparison of satellite AOD datasets for
1173 aerosol model evaluation, *Atmos. Chem. Phys.*, 20, 12431–12457,
1174 <https://doi.org/10.5194/acp-20-12431-2020>, 2020.

1175 Sharma, V., Ghosh, S., Bilal, M., Dey, S., and Singh, S.: Performance of MODIS C6 . 1 Dark
1176 Target and Deep Blue aerosol products in Delhi National Capital Region , India : Application
1177 for aerosol studies, *Atmos. Pollut. Res.*, 12, 65–74, <https://doi.org/10.1016/j.apr.2021.01.023>,
1178 2021.

1179 Shaw, G. E., Reagan, J. A., and Herman, B. M.: Investigations of Atmospheric Extinction
1180 Using Direct Solar Radiation Measurements Made with a Multiple Wavelength Radiometer,
1181 *J. Appl. Meteorol.*, 12, 374–380, [https://doi.org/10.1175/1520-0450\(1973\)012<0374:IOAEUD>2.0.CO;2](https://doi.org/10.1175/1520-0450(1973)012<0374:IOAEUD>2.0.CO;2), 1973.

1182 Shi, Y., Li, L., and Zhang, L.: Application and comparing of IDW and Kriging interpolation
1183 in spatial rainfall information, in: *Geoinformatics 2007: Geospatial Information Science*,
1184 67531I, <https://doi.org/10.1117/12.761859>, 2007.

1185 Sifaou, H., Kammoun, A., and Alouini, M. S.: A Precise Performance Analysis of Support
1186 Vector Regression, *Proc. Mach. Learn. Res.*, 139, 9671–9680, 2021.

1187 Singh, M. K. and Venkatachalam, P.: Merging of aerosol optical depth data from multiple
1188 remote sensing sensors, in: *2014 IEEE Geoscience and Remote Sensing Symposium*, 4173–
1189 4175, <https://doi.org/10.1109/IGARSS.2014.6947407>, 2014.

1190 Singh, M. K., Gautam, R., and Venkatachalam, P.: A merged aerosol dataset based on
1191 MODIS and MISR Aerosol Optical Depth products, *Remote Sens. Atmos. Clouds, Precip.*
1192 *VI*, 9876, 987627, <https://doi.org/10.1117/12.2223485>, 2016.

1193 Singh, P. and Verma, P.: A comparative study of spatial interpolation technique (IDW and
1194 Kriging) for determining groundwater quality, in: *GIS and Geostatistical Techniques for*
1195 *Groundwater Science*, Elsevier, 43–56, <https://doi.org/10.1016/B978-0-12-815413-7.00005-5>,
1196 2019.

1197 Singh, P., Vaishya, A., Rastogi, S., and Babu, S. S.: Seasonal heterogeneity in aerosol optical
1198 properties over the subtropical humid region of northern India, *J. Atmos. Solar-Terrestrial*
1199 *Phys.*, 201, <https://doi.org/10.1016/j.jastp.2020.105246>, 2020.

1200 Sinha, P. R., Dumka, U. C., Manchanda, R. K., Kaskaoutis, D. G., Sreenivasan, S., Krishna
1201 Moorthy, K., and Suresh Babu, S.: Contrasting aerosol characteristics and radiative forcing
1202 over Hyderabad, India due to seasonal mesoscale and synoptic-scale processes, *Q. J. R.*
1203 *Meteorol. Soc.*, 139, 434–450, <https://doi.org/10.1002/qj.1963>, 2013.

1204 Sivadasan Nair, V., Giorgi, F., and Keshav Hasyagar, U.: Amplification of South Asian haze
1205 by water vapour-aerosol interactions, *Atmos. Chem. Phys.*, 20, 14457–14471,
1206 <https://doi.org/10.5194/acp-20-14457-2020>, 2020.

1207 Smola, A. and Schölkopf, B.: A tutorial on support vector regression, *Stat. Comput.*, 14, 199–
1208 222, <https://doi.org/10.1023/B%3ASTCO.0000035301.49549.88>, 2004.

1209 Snepvangers, J. J. J. C., Heuvelink, G. B. M., and Huisman, J. A.: Soil water content
1210 interpolation using spatio-temporal kriging with external drift, *Geoderma*, 112, 253–271,
1211 [https://doi.org/10.1016/S0016-7061\(02\)00310-5](https://doi.org/10.1016/S0016-7061(02)00310-5), 2003.

1212 Sogacheva, L., Popp, T., Sayer, A. M., Dubovik, O., Garay, M. J., Heckel, A., Christina Hsu,
1213 N., Jethva, H., Kahn, R. A., Kolmonen, P., Kosmale, M., De Leeuw, G., Levy, R. C.,
1214

1215 Litvinov, P., Lyapustin, A., North, P., Torres, O., and Arola, A.: Merging regional and global
1216 aerosol optical depth records from major available satellite products, *Atmos. Chem. Phys.*,
1217 20, 2031–2056, <https://doi.org/10.5194/acp-20-2031-2020>, 2020.

1218 Stein, A. and Corsten, L. C. A.: Universal Kriging and Cokriging as a Regression Procedure,
1219 *Biometrics*, 47, 575, <https://doi.org/10.2307/2532147>, 1991.

1220 Subba, T., Gogoi, M. M., Moorthy, K. K., Bhuyan, P. K., Pathak, B., Guha, A., Srivastava,
1221 M. K., Vyas, B. M., Singh, K., Krishnan, J., Lakshmikummar, T. V. S., and Babu, S. S.:
1222 Aerosol Radiative Effects Over India from Direct Radiation Measurements and Model
1223 Estimates, *SSRN Electron. J.*, <https://doi.org/10.2139/ssrn.3986898>, 2021.

1224 Tandule, C. R., Gogoi, M. M., Gouda, S. S., and Suresh Babu, S.: Retrieval of aerosol optical
1225 depth from INSAT-3DR for accurate geostationary monitoring of regional and temporal
1226 aerosol dynamics, *Atmos. Environ.*, 367, 121730,
1227 <https://doi.org/https://doi.org/10.1016/j.atmosenv.2025.121730>, 2026.

1228 Tang, Q., Bo, Y., and Zhu, Y.: Spatiotemporal fusion of multiple-satellite aerosol optical
1229 depth (AOD) products using bayesian maximum entropy method, *J. Geophys. Res.*, 121,
1230 4034–4048, <https://doi.org/10.1002/2015JD024571>, 2016.

1231 Tao, M., Wang, J., Li, R., Chen, L., Xu, X., Wang, L., Tao, J., Wang, Z., and Xiang, J.:
1232 Characterization of Aerosol Type Over East Asia by 4.4 km MISR Product: First Insight and
1233 General Performance, *J. Geophys. Res. Atmos.*, 125, <https://doi.org/10.1029/2019JD031909>,
1234 2020.

1235 Tao, M., Chen, J., Xu, X., Man, W., Xu, L., Wang, L., Wang, Y., Wang, J., Fan, M., Shahzad,
1236 M. I., and Chen, L.: A robust and flexible satellite aerosol retrieval algorithm for multi-angle
1237 polarimetric measurements with physics-informed deep learning method, *Remote Sens.*
1238 *Environ.*, 297, 113763, <https://doi.org/https://doi.org/10.1016/j.rse.2023.113763>, 2023.

1239 Tian, X. and Gao, Z.: Validation and Accuracy Assessment of MODIS C6.1 Aerosol Products
1240 over the Heavy Aerosol Loading Area, *Atmosphere (Basel)*, 10,
1241 <https://doi.org/10.3390/atmos10090548>, 2019.

1242 Tian, X., Liu, Q., Li, X., and Wei, J.: Validation and comparison of MODIS C6.1 and C6
1243 aerosol products over Beijing, China, *Remote Sens.*, 10, <https://doi.org/10.3390/rs10122021>,
1244 2018.

1245 Tiwari, S., Kaskaoutis, D., Soni, V. K., Dev Attri, S., and Singh, A. K.: Aerosol columnar
1246 characteristics and their heterogeneous nature over Varanasi, in the central Ganges valley,
1247 *Environ. Sci. Pollut. Res.*, 25, 24726–24745, <https://doi.org/10.1007/s11356-018-2502-4>,
1248 2018.

1249 Vieira, S., Carvalho, J., Ceddia, M., and Paz-González, A.: Detrending non stationary data for
1250 geostatistical applications, *Bragantia*, 69, 1–8, <https://doi.org/10.1590/S0006-87052010000500002>, 2009.

1251 Viswanatha Vachaspati, C., Reshma Begam, G., Nazeer Ahammed, Y., Raghavendra Kumar,
1252 K., and Reddy, R. R.: Characterization of aerosol optical properties and model computed
1253 radiative forcing over a semi-arid region, Kadapa in India, *Atmos. Res.*, 209, 36–49,
1254 <https://doi.org/10.1016/j.atmosres.2018.03.013>, 2018.

1255 Wang, H., Zhang, R., Liu, K., Wang, G., Liu, W., and Li, N.: Improved Kriging interpolation
1256 based on support vector machine and its application in oceanic missing data recovery, in:
1257 *Proceedings - International Conference on Computer Science and Software Engineering*,
1258 *CSSE 2008*, 726–729, <https://doi.org/10.1109/CSSE.2008.924>, 2008.

1259 Wang, Y., You, Z., Wang, L., Wang, J., Zhou, M., Tao, M., and Kim, J.: First high temporal
1260 resolution retrievals of AOD over shallow and turbid coastal waters for Himawari-8, *ISPRS J.*
1261 *Photogramm. Remote Sens.*, 228, 603–612,
1262 <https://doi.org/https://doi.org/10.1016/j.isprsjprs.2025.07.027>, 2025a.

1263 Wang, Z., Su, X., Wang, L., Lang, Q., Lu, Y., and Wang, L.: A Physics-Guided Neural
1264 Network Model to Estimate All-Sky Diffuse Solar Radiation Using Himawari-8 Data, *IEEE*
1265

1266 Trans. Geosci. Remote Sens., 63, 1–18, <https://doi.org/10.1109/TGRS.2025.3543883>, 2025b.
1267 Wei, J., Li, Z., Sun, L., Peng, Y., and Wang, L.: Improved merge schemes for MODIS
1268 Collection 6.1 Dark Target and Deep Blue combined aerosol products, Atmos. Environ., 202,
1269 315–327, <https://doi.org/10.1016/j.atmosenv.2019.01.016>, 2019.
1270 Witek, M. L., Garay, M. J., Diner, D. J., Bull, M. A., and Seidel, F. C.: New approach to the
1271 retrieval of AOD and its uncertainty from MISR observations over dark water, Atmos. Meas.
1272 Tech., 11, 429–439, <https://doi.org/10.5194/amt-11-429-2018>, 2018.
1273 Witek, M. L., Garay, M. J., Diner, D. J., Bull, M. A., Seidel, F. C., Nastan, A. M., and
1274 Hansen, E. G.: Introducing the MISR level 2 near real-time aerosol product, Atmos. Meas.
1275 Tech., 14, 5577–5591, <https://doi.org/10.5194/amt-14-5577-2021>, 2021.
1276 Wong, M. S., Shahzad, M. I., Nichol, J. E., Lee, K. H., and Chan, P. W.: Validation of
1277 MODIS, MISR, OMI, and CALIPSO aerosol optical thickness using ground-based
1278 sunphotometers in Hong Kong, Int. J. Remote Sens., 34, 897–918,
1279 <https://doi.org/10.1080/01431161.2012.720739>, 2013.
1280 Xu, H., Xue, Y., Guang, J., Li, Y., Yang, L., Hou, T., He, X., Dong, J., and Chen, Z.: A semi-
1281 empirical optical data fusion technique for merging aerosol optical depth over China, in: 2012
1282 IEEE International Geoscience and Remote Sensing Symposium, 2524–2527,
1283 <https://doi.org/10.1109/IGARSS.2012.6350338>, 2012.
1284 Zhang, F. and O'Donnell, L. J.: Support vector regression, in: Machine Learning, Elsevier,
1285 123–140, <https://doi.org/10.1016/B978-0-12-815739-8.00007-9>, 2020.
1286 Zhao, A., Li, Z., Zhang, Y., Zhang, Y., and Li, D.: Merging MODIS and ground-based fine
1287 mode fraction of aerosols based on the geostatistical data fusion method, Atmosphere
1288 (Basel), 8, <https://doi.org/10.3390/atmos8070117>, 2017.
1289 Zhou, Y., Scavia, D., and Michalak, A. M.: Nutrient loading and meteorological conditions
1290 explain interannual variability of hypoxia in Chesapeake Bay, Limnol. Oceanogr., 59, 373–
1291 384, <https://doi.org/10.4319/lo.2014.59.2.0373>, 2014.
1292 Zimmerman, D., Pavlik, C., Ruggles, A., and Armstrong, M. P.: An experimental comparison
1293 of ordinary and universal kriging and inverse distance weighting, Math. Geol., 31, 375–390,
1294 <https://doi.org/10.1023/A:1007586507433>, 1999.
1295